# Triply stimuli-responsive mitochondria-targeting supramolecular nanodrugs co-assembled mainly by electrostatic attraction for enhanced chemo-photothermal combination therapy

Yu Cheng, Yuanhui Ji, Jiwei Tong

PII: S0168-3659(20)30437-5

DOI: https://doi.org/10.1016/j.jconrel.2020.08.006

Reference: COREL 10449

To appear in: *Journal of Controlled Release*

Received date: 10 April 2020

Revised date: 27 June 2020

Accepted date: 4 August 2020

Please cite this article as: Y. Cheng, Y. Ji and J. Tong, Triply stimuli-responsive mitochondria-targeting supramolecular nanodrugs co-assembled mainly by electrostatic attraction for enhanced chemo-photothermal combination therapy, *Journal of Controlled Release* (2020), https://doi.org/10.1016/j.jconrel.2020.08.006

# Triply stimuli-responsive mitochondria-targeting supramolecular nanodrugs co-assembled mainly by electrostatic attraction for enhanced chemo-photothermal combination therapy

Yu Cheng, Yuanhui Ji*, Jiwei Tong

*Jiangsu Province Hi-Tech Key Laboratory for Biomedical Research, School of Chemistry and Chemical Engineering, Southeast University, Nanjing, 211189, P.R. China*

* Corresponding author: Tel: +86-13951907361; Email: yuanhui.ji@seu.edu.cn; yuanhuijinj@163.com.

**Abstract:**

Mitochondria play crucial roles in a variety of cellular physiological processes, mitochondria-accumulating drug delivery has drawn pronounced attention in the field of cancer theranostics. Camptothecin (CPT) is a DNA Topoisomerase I inhibitor and exerts a broad-spectrum anticancer profile. Berberine (BBR) is able to perferably enter into cancer cell mitochondria and trigger the cell apoptosis. In this work, CPT and BBR were combined together (CPT-ss-BBR) through GSH-responsible disulfide bond, and then co-assembled with photosensitizer indocyanine green (ICG) into nanodrugs (CPT-ss-BBR/ICG NPs), which was driven through hydrophobic, π-π stacking and especially, electrostatic interactions of anions and cations as found by molecular dynamics simulations and quantum chemistry calculations. Our developed nanodrugs displayed an average size of ~168 nm and showed exceptional instability by irradiation presence, acid condition and high concentration of GSH, thereby eliciting the rapid disassembly and accelerating drug release. The better therapy effect of CPT-ss-BBR/ICG NPs on A549 cells might be attributed to triply stimuli-responsive rapid disassembly, preferable accumulation into mitochondria and combined chemotherapy and photothermal therapy, all of which directly rendered the notable loss of mitochondria membrane potential, high level of reactive oxygen species in cancer cells, accelerated the apoptosis of cancer cells and repressed the growth of tumors.

**Keywords:** mitochondria-targeting; co-assembly nanodrug; camptothecin; indocyanine green; berberine

## 1. Introduction

To combat the serious health concern worldwide by neoplastic diseases and promote the effective delivery of a drug to its action site, nanotechnology-based strategies have been extensively explored due to its advantage of improved drug bioavailability, preferential tumor specificity and enhanced treatment efficiency to the disease.[1,2] The design and preparation of nanodrugs often involves the participation of nanocarriers, including liposomes[3], vesicles[4], nanogels[5], polymeric nanoparticles[6], nanoemulsions[7], and inorganic particles[8], and a variety of which have been successfully developed to delivery drugs with the approach of physical entrapment or chemical conjugation.

Although a large number of nanodrug delivery systems have been gained, there have been only a few approved by the FDA and entered into the clinic practice.[9] This can be put down to the certain inevitable circumstances, that the nanocarriers needed for delivering drugs exhibit low capacity of drug bearing[10] and may cause cancer cell metastasis[11] and short-term and long-term toxicities to kidneys or other organs during the process of degradation, metabolism, and excretion.[12,13] Therefore, the exploration of rational, simple, and repeatable approaches to fabricate carrier-free nanoplatforms with excellent stability and desirable bioactivity remains a tremendous challenge in biomedical science and has the vital practical significance in clinical medicine. Supramolecular assembly based on intermolecular interactions (e.g., electrostatic, $\pi$-$\pi$ stacking, hydrophobic interactions and hydrogen bond), especially the co-assembly of diverse drug entities into versatile nanodrugs has attracted wide attention with the advantages of regulative functionality, structural diversity, therapeutic cooperativity, apart from improving the water solubility and passive-targeting drug delivery.[14-16]

Among the organelles of mammalian cells, double-membrane-structured mitochondria as cell energy stations play crucial roles in cell signal transduction, cell growth, cell death and material metabolism.[17] When normal cells become carcinogenic, the “cell power plant” become dysfunctional and express a higher level of reactive oxygen species (ROS) and reductants (e.g., GSH) and more negative charged transmembrane potential.[18] Hence, mitochondria-targeting drug delivery platforms have attracted increased attention and are promising to provide enhanced drug uptake and increased therapeutic effect. As mitochondria-homing moieties, delocalized lipophilic cations (DLCs) are more preferential to accumulate into the mitochondria of tumor cells than normal cells, which is induced by the mitochondrial membrane potential discrepancy between tumor cells ($\Delta\Psi$, ~−220 mV) and normal cells ($\Delta\Psi$, ~−140 mV).[19,20] Berberine (BBR) is an isoquinoline alkaloid derived from herbal plants named ‘Huang Lian’ in Chinese and has been reported for the treatment of atherosclerosis[21], colitis[22], diabetes mellitus[23], hyperlipidemia[24]. Remarkably, berberine has an amphiphilic delocalized positive charge structure, which imparts its capacity for selectively accumulation into the tumor cell mitochondria.[25-27] Moreover, berberine is also able to inhibit the proliferation and result in the apoptosis of various cancers, by inducing the loss of mitochondrial membrane potential, the elevation of ROS levels and triggering mitochondrial dysfunction.[28-30]

Camptothecin (CPT) and its analogs bind to eukaryotic DNA Topoisomerase I (Top I) and have been extensively studied as DNA Top I inhibitors.[31] To date, there are several camptothecin derivates approved by the FDA, which have been widely used for treating cervical cancer, ovarian cancer, and small-cell lung cancer in clinic. Despite great advances achieved, multidrug resistance

(MDR) has been prevalent in campothecins.[32] A primary cause of MDR occurrence is often related to the chemotherapeutic drug efflux by the adenosine triphosphate (ATP)-binding cassette transporters such as P-glycoprotein (P-gp), which reduces the concentration of the agents in the tumor cells, making it difficult to achieve a therapeutic effect.[33] Some reports have also found that CPT can act as a cellular respiration inhibitor to stimulate endogenous mitochondrial ROS production and reduce mitochondrial membrane potential, apart from the general inhibition of DNA Top I for cancer therapy.[34-37] Hence, targeted delivery of camptothecin to the mitochondria from cancer cells is expected to overcome drug resistance while improving the chemotherapy effect.

In addition, despite the huge contribution of chemotherapy clinically, the strategy is still struggling with the shortcomings due to its severe side effects and repeated relapses and metastases of diseases. In order to address the current dilemmas in chemotherapy, with the continuous and vigorous advancement of nanotechnology, combination therapy, which refers to the integration of two or more treatment strategies, has been established as a promising approach, and recently, many studies have gradually shifted from a focus on monotherapy to combination therapy, which may lead to increase therapeutic effects and overcome respective drawbacks.[38-40] A usual tactic is to combine photothermal therapy (PTT) with chemotherapy. PTT as a non-invasive therapy can convert absorbed near-infrared (NIR) optical energy into thermal energy to induce irreversible destruction of tumor cells and can maximize therapeutic effect with lesser systemic toxicity to normal tissues through administration of a lower drug dosage.[41,42]

Encouraged by above observations and our previous work[30], considering the outstanding mitochondria-homing characteristic and potential synergetic anticancer effect of berberine, the clinically general acceptance of camptothecin, the particular light-thermal conversion feature of indocyanine green (ICG) and the high level of glutathione (GSH) in mitochondria from carcinoma cells[18], in this work, we employed camptothecin with berberine to construct a new stimuli-responsive conjugate (CPT-ss-BBR), which was able to co-assembly with ICG and came into being steady and versatile nanodrugs (CPT-ss-BBR/ICG NPs). The systhesis of CPT-ss-BBR conjugate was illustrated in Scheme 1. The formation of nanodrugs was mainly driven through electrostatic interactions as found by computational approaches. The better therapy effect of CPT-ss-BBR/ICG NPs on A549 cells might be attributed to triply stimuli-responsive rapid disassembly, preferable accumulation into mitochondria and combined chemotherapy and photothermal therapy (Fig. 1).

**Figure 1**

**Fig. 1.** Schematic illustration of the preparation of NIR/GSH/pH-sensitive CPT-ss-BBR/ICG NPs and chemo-photothermal synergistic therapy process of nanodrugs.

## 2. Materials and methods

### *2.1. Materials*

Glutathione (GSH), acetonitrile ($CH_3CN$), berberine hydrochloride, camptothecin and methanol ($CH_3OH$) were supplied by Shanghai Adamas Reagent Co., Ltd. (Shanghai, China). *N*,*N*-dicyclohexylcarbodiimide (DCC), 3,3-dithiodipropionic acid, 4-dimethylaminopyridine (DMAP), 3-(4,5-dimethyl-2-tetrazolyl)-2,5-diphenyltetrazolium bromide (MTT), *N*-bromosuccinimide (NBS), potassium carbonate ($K_2CO_3$), sodium borohydride ($NaBH_4$) and chloroform ($CHCl_3$) were obtained from Nanjing Wanqing Chemical Glassware Istrument Co., Ltd. (Nanjing, China) or Nanjing Juyou Scientific Equipment Co., Ltd. (Nanjing, China). Indocyanine green (ICG) was bought from Aladdin Co., Ltd. (Shanghai, China). Annexin V-FITC/PI apoptosis detection kit and Mitotracker Red were purchased from Jiangsu KeyGEN Biotech Co., Ltd. (Nanjing, China).

### *2.2. Chemistry synthesis of CPT-ss-BBR conjugate*

Compounds **2**, **3** and **4** were synthesized as a previously described method.[30] Briefly, berberine (**1**, 5.0 g, 13.47 mmol) was selectively demethylated at 9-position under high temperature and vacuum conditions to obtain red-brown compound **2** (3.68 g, yield = 85%), which was further reacted with bromoethanol in potassium carbonate as the base to gain compound BBR-OH as yellow solid with more than 80% yield. The intermediate **4** (3.06 g) was produced by the $NaBH_4$ (0.76 g, 20.14 mmol) reduction of compound **3** (4.48 g, 10.07 mmol) in methanol and it was light-yellow solid with 82% yield.

Synthesis of compound **6**: 3,3'-Dithiodipropionic acid (2.00 g, 9.51 mmol) was stirred in acetyl chloride (20 mL) and then refluxed at 60 $^oC$ for 3 h. After the reaction was completed, the solvent was removed and the residue was precipitated in excess ice-diethyl ether to obtain dithiodipropionic anhydride. The 10 mL pyridine solution of DMAP (0.16 g, 1.29 mmol) was added dropwise to a solution of CPT (0.45 g, 1.29 mmol) and dithiodipropionic anhydride (1.24 g, 6.45 mmol) in 40 mL dry pyridine at ice bath under nitrogen protection. The mixture was heated to reflux, and then the reaction was continued for 48 hours. After the reaction was completed, the reaction solution was extracted with dilute hydrochloric acid and chloroform, and then was purified by silica gel column chromatography (eluent: $CHCl_3/CH_3OH$ = 20/1, V/V) to gain white compound **6** (0.51 g, yield = 73%).

Synthesis of compound **7**: Compound **4** (0.90 g, 2.43 mmol) in dry pyridine (10 mL) was added little by little to a dry pyridine solution (20 mL) of DCC (1.00 g, 4.86 mmol), compound **6** (1.31 g, 2.43 mmol) and DMAP (0.15 g, 1.22 mmol) under nitrogen protection. The mixture was reacted at 0 °C for 48 h, and then the residual solvent was removed under reduced pressure. The crude product was purified by silica gel column chromatography (eluent: $CHCl_3$/$CH_3OH$ = 45/1, V/V) to gain the pure light-yellow compound **7** (1.84 g, yield = 85%). $^1$H NMR (600 MHz, $CDCl_3$) δ 8.38 (s, 1H), 8.22 (d, *J* = 5.7 Hz, 1H), 7.93 (d, *J* = 5.5 Hz, 1H), 7.82 (t, *J* = 5.5 Hz, 1H), 7.66 (t, *J* = 5.0 Hz, 1H), 7.26 (s, 1H), 6.86 (d, *J* = 5.6 Hz, 1H), 6.77 (d, *J* = 5.6 Hz, 1H), 6.70 (s, 1H), 6.57 (s, 1H), 5.91 (s, 2H), 5.67 (d, *J* = 11.4 Hz, 1H), 5.40 (d, *J* = 11.4 Hz, 1H), 5.29 – 5.27 (m, 2H), 4.36 (dd, *J* = 7.1, 3.3 Hz, 2H), 4.24 (dd, *J* = 5.7, 2.4 Hz, 2H), 4.17 (dd, *J* = 5.2, 2.3 Hz, 1H), 3.81 (s, 3H), 3.48 (s, 2H), 3.21 (d, *J* = 7.2 Hz, 3H), 3.02 – 2.88 (m, 7H), 2.78 (t, *J* = 4.8 Hz, 2H), 2.70 – 2.56 (m, 2H), 2.28 (dd, *J* = 9.7, 4.6 Hz, 1H), 2.16 (dd, *J* = 9.4, 5.0 Hz, 1H), 0.98 (t, *J* = 5.0 Hz, 3H).; HRMS (ESI) calcd. for $C_{47}H_{45}N_3O_{11}S_2$ $[M+H]^+$, 892.2574; found, 892.25649.

Synthesis of CPT-ss-BBR conjugate **8**: NBS (0.11 g, 0.60 mmol) in dry $CHCl_3$ (2 mL) was added dropwise to a dry $CHCl_3$ (15 mL) of compound **7** (0.45 g, 0.50 mmol) and reacted at 50 °C for 6 h. The crude product was purified by silica gel column chromatography (eluent: $CHCl_3$/$CH_3OH$ = 8/1, V/V) to gain the pure yellow compound **8** (0.23 g, yield = 48%). $^1$H NMR (600 MHz, DMSO-$d_6$, ppm): δ 9.70 (s, 1H), 8.83 (s, 1H), 8.65 (s, 1H), 8.16 (d, *J* = 6.1 Hz, 1H), 8.05 (dd, *J* = 12.5, 5.5 Hz, 2H), 7.94 (d, *J* = 6.1 Hz, 1H), 7.77 (t, *J* = 5.1 Hz, 1H), 7.70 (s, 1H), 7.64 (t, *J* = 5.0 Hz, 1H), 7.13 (s, 1H), 6.96 (s, 1H), 6.18 (s, 2H), 5.50 – 5.41 (m, 2H), 5.23 (d, *J* = 2.8 Hz, 2H), 4.89 – 4.85 (m, 2H), 4.48 (dd, *J* = 7.0, 3.7 Hz, 2H), 4.43 (dd, *J* = 6.5, 4.3 Hz, 2H), 4.03 (s, 3H), 3.15 – 3.11 (m, 2H), 3.00 – 2.90 (m, 6H), 2.77 (t, *J* = 4.5 Hz, 2H), 2.12 (dt, *J* = 7.1, 4.7 Hz, 2H), 0.91 (t, *J* = 4.9 Hz, 3H).; HRMS (ESI) calcd. for $C_{47}H_{42}N_3O_{11}S_2$ $[M-Br]^+$, 888.2255; found, 888.22594.

### *2.3. Preparation and characterization of CPT-ss-BBR/ICG NPs*

We prepared the CPT-ss-BBR/ICG NPs using a nano-precipitation method. In detail, a 0.4 mL DMSO solution of CPT-ss-BBR conjugate (10 mg, 0.01 mmol) and ICG (8 mg, 0.01 mmol) was added dropwise into the 10 mL deionized water and the mixed system was stirred 2 h to form the co-assembled nanomedicine CPT-ss-BBR/ICG NPs. Then, the solution was dialyzed (MWCO = 3500 Da) against deionized water for 12 h to remove DMSO.

The transmission electron microscopy (TEM, JEM-2100F, JEOL) and dynamic light scattering (DLS, Malvern Zetasizer Nano-ZS90, Malvern) were employed for checking morphological observation and detecting size and size distribution of CPT-ss-BBR/ICG NPs. The UV spectra of the samples were determined by a UV-vis spectrophotometer (Lambda365, PerkinElmer) with the scanning range from 250 to 1000 nm. The intensity of scattered light (Kcps) of a series of solutions of CPT-ss-BBR was monitored and the critical micelle concentration was the crosspoint when extrapolating the intensity in the low and high concentration ranges.

### *2.4. Computational simulations*

Molecular dynamics (MD) simulations were performed for CPT-ss-BBR conjugate and ICG using GROMACS 5.1.4 package with GAFF force field. The force field parameters of CPT-ss-BBR conjugate and ICG were generated using Gaussian 09 package and AmberTools15. The system was solvated with SPC water model, in a cubic box with periodic boundary condition. $Na^+$ or $Cl^-$ counterions were added to achieve overall charge neutrality. Simulations were performed with the pressure fixed at 1 atm and temperature at 300 K. The energy minimization was carried out with 5000 steps of steepest descent, followed by equilibration under NVT and NPT ensembles with position restrain on CPT-ss-BBR conjugate and ICG for 500 ps. After the system attained an equilibrated state, 50 or 100 ns MD simulation was carried out with a time step of 2 fs and frames saved at every 10 ps. The resulting trajectory files were analyzed using Gromacs gmx-toolbox. Gaussian 09 package was employed to perform analyses the electrostatic potential (ESP). Optimization of the structures and frequency analysis were calculated by using the B3LYP/6-31G functional.

### *2.5. In vitro photothermal effect test*

Four hundred microliters of PBS, free ICG or CPT-ss-BBR/ICG NPs solution with determined concentration of ICG were, respectively, irradiated with the 808 nm laser (1 or 2 $W/cm^2$) for 5 min and used a FLIR TG165 thermal imager and PT1000 temperature sensor to record temperature changes simultaneously.

### *2.6. In vitro drug release*

The drug release tests of CPT-ss-BBR/ICG NPs were performed *via* dialysis. 1 mL of co-assembly solution was put into the dialysis bag (MWCO = 3500 Da), and then immersed into 30 mL phosphate buffer solution (PBS) (pH = 7.4 or 5.6, with or without 20 mM GSH, with or without 808 nm laser irradiation) in a shaking bed (ratio = 150 rpm) at 37 °C. The amount of drug released was detected using a UV-vis spectrophotometer (Lambda365, PerkinElmer). Data were given as mean ± standard deviation (SD, n = 3).

### *2.7. Cell culture*

China Pharmaceutical University (Nanjing, China) provided A549 cell (a human lung adenocarcinoma cell line), which was cultured in RPMI-1640 medium complemented with 10% FBS and antibiotics (50 units/mL streptomycin and 50 units/mL penicillin) with a humidified incubator containing 5% $CO_2$.

### *2.8. In vitro cytotoxicity assay*

The MTT method was used to evaluate the cytotoxicity of nanodrugs. In brief, the A549 cells were seeded in 96-well plates ($2\times10^4$ cells/well) for 24 h. Then, the cells were incubated with fresh culture medium containing CPT-ss-BBR/ICG NPs, CPT-ss-BBR, CPT, BBR-OH and ICG at tested concentrations of 0.625, 1.25, 2.5, 5, 10, 20 and 40 μM. After 24, 48 or 72 h, the culture solutions were removed and the cells were washed with PBS. Then, 25 μL 5% MTT was added to each well. After treatment for 4 h, 150 μL DMSO was used to extract the formazan products for 10 min and the absorption of solution was measured by microplate-680 reader (Bio-Rad, CA) at 570 nm for the calculation of cell viability. The cell viability was calculated as follows: cell viability (%) = ($OD_{test}$-$OD_{blank}$) / ($OD_{control}$-$OD_{blank}$) × 100, where $OD_{test}$ was the absorbance at the presence of sample solutions, $OD_{blank}$ was the absorbance of blank plates and $OD_{control}$ was the absorbance without treatment. Each group was performed in three independent measurements and the half-maximal inhibitory concentration ($IC_{50}$) value was calculated using GraphPad Prism software. For photocytotoxicity effect of nanodrugs, A549 cells were treated with the same concentrations of CPT-ss-BBR/ICG NPs and ICG at 37 $^{o}$C. Then, the cells were illuminated with a laser for 5 min at 808 nm (1 W/cm$^2$). The following experimental steps were consistent with the previous case.

*2.9. Calcein-AM/PI staining*

Approximately 1 × 10$^4$ A549 cells were cultured in glass-bottomed dish for 24 h. Cells were then exposed to a CPT-ss-BBR/ICG NPs (with or without laser), CPT-ss-BBR, CPT, BBR-OH and ICG (with or without laser) patch with a dose of 20 μM for 6 h. The laser irradiation groups were irradiated with 808 nm laser for 5 min at 1 W/cm$^2$, and dead cells were detected with a Calcein-AM/PI kit (Jiangsu KeyGEN, Nanjing, China) for 30 min according to the manufacturer's instructions. Next, the images were captured by confocal laser scanning microscope (CLSM).

*2.10. Apoptosis effect in vitro*

The apoptosis of A549 cells was detected using Annexin V-FITC/PI apoptosis detection kit (Jiangsu KeyGEN, Nanjing, China). The cells (1×10$^4$ cells per dish) were seeded in 6-well plates. After culture for 12 h, the cells were respectively treated with PBS, 40 μM of CPT-ss-BBR/ICG NPs (with or without laser), CPT-ss-BBR, CPT, BBR-OH and ICG (with or without laser) for 24 h. The laser irradiation groups were illuminated with a laser for 5 min at 808 nm (1 W/cm$^2$). The subsequent procedures were performed according to the manufacturer's suggested procedures. The cells were analyzed by FACScan flow cytometer.

*2.11. Mitochondrial targeting*

A549 cells were seeded into glass-bottomed dish at a density of 1 × 10$^4$ cells per dish. After culture for 12 h, the cells were treated with 5 μM of BBR-OH, CPT-ss-BBR and CPT-ss-BBR/ICG NPs at 37 °C for predesigned incubation time periods. Subsequently, the cells were stained by 1 μM of Mitotracker Red at 37 °C for 25 min. Finally, the cells were washed by cold PBS twice and immediately observed using CLSM.

*2.12. Statistical analysis*

Data were expressed as the mean ± SD on three independent measurements. One-way analysis (ANOVA) by GraphPad Prism software was used to evaluate the statistical significance.

## 3. Results

### *3.1. Chemistry synthesis of CPT-ss-BBR conjugate*

The conjugate CPT-ss-BBR (**8**) was synthesized *via* six steps according to Scheme 1. Firstly, compound **3** (**BBR-OH**) was obtained by a simple and general method. Briefly, berberine (**1**) was selectively demethylated at 9-position under high temperature and vacuum conditions to obtain compound **2**, which was further reacted with bromoethanol in potassium carbonate as the base to gain compound **BBR-OH**. The intermediate **4** was produced by the $NaBH_4$ reduction of compound **3** in methanol. CPT-ss-COOH (**6**) was gained by the esterification of dithiodipropionic anhydride with camptothecin (**5**). Compound **6** and intermediate **4** were condensed to reveive a conjugated prodrug compound **7**, which was ulteriorly oxidized to prepare target camptothecin-ss-berberine (CPT-ss-BBR, **8**). Targeted conjugate CPT-ss-BBR and key intermediates were confirmed by $^1$H NMR, and HRMS spectra.

**Scheme 1**

**Scheme 1**. Synthetic scheme of stimuli-responsive CPT-ss-BBR conjugate.

Reagents and conditions: i) 190 $^{o}$C/vacuo; ii) $K_2CO_3$, $CH_3CN$, bromoethanol, reflux, 24 h; iii) $NaBH_4$, $CH_3OH$, 0 $^{o}$C; iv) dithiodipropionic anhydride, pyridine, DMAP, 0 $^{o}$C, 48 h; v) compound **4**, pyridine, DCC, DMAP, 0 $^{o}$C; vi) NBS, $CHCl_3$, 50 $^{o}$C.

### *3.2. Characterization of CPT-ss-BBR/ICG NPs*

The morphology and size distribution of the CPT-ss-BBR/ICG nanodrugs were characterized using TEM and DLS. As shown in the TEM image of Fig. 2A, the CPT-ss-BBR/ICG NPs had an unusually spherical shape with a size of about 150 nm. DLS measurements showed that the mean size of the nanodrugs was approximately 168 nm (Fig. 2C) with a narrow polydispersity index (PDI = 0.086) and the critical micelle concentration was determined to be CMC = 2.29 μM (Fig. 2E). After the nanodrugs were treated with high concentration of GSH for 5 h, obvious dissociation occurred (Fig. 2B), which verified its reduction responsiveness and was helpful for stimulating drug release. However, under PBS or PBS including 10% fetal bovine serum (FBS) conditions, the CPT-ss-BBR/ICG NPs were very stable, and the particle size had hardly changed for up to 20 days (Fig. 2C and 2D). The UV-vis absorption spectra of CPT-ss-BBR/ICG NPs, CPT-ss-BBR, and free ICG were measured at 250~1000 nm (Fig. 2F). Compared with CPT-ss-BBR conjugate and free ICG, absorption curve of nanodurgs had a significant red shift and the absorption peaks become broader, which implied that there was a strong interaction between CPT-ss-BBR and free ICG and that the CPT-ss-BBR/ICG NPs had been successfully constructed.

**Figure 2**

**Fig. 2.** (A) Morphology image of CPT-ss-BBR/ICG NPs in PBS (pH = 7.4). (B) Morphology image of CPT-ss-BBR/ICG NPs harvested with 20 mM GSH for 5h. (C) Size distribution of CPT-ss-BBR/ICG NPs in PBS (pH = 7.4) or in PBS (pH = 7.4) with FBS at 0 or 20 days. (D) Variations of size of CPT-ss-BBR/ICG NPs in PBS (pH = 7.4) or in PBS (pH = 7.4) with FBS for 20 days. (E) The light scattering intensities (Kcps) of aqueous solutions containing different concentrations CPT-ss-BBR/ICG NPs. (F) UV-vis spectra of CPT-ss-BBR, CPT-ss-BBR/ICG NPs and free ICG.

### *3.3. Co-assembly mechanism of CPT-ss-BBR/ICG NPs by computational simulations*

Computational simulation technology has shown to be a useful strategy to study the supramolecular assembly behavior of complex systems, especially to probe early stages of dynamics and mechanism of aggregation.[43,44] In order to reveal how the intermolecular forces to stabilize the CPT-ss-BBR/ICG NPs and considering the aggregation of two molecules as the smallest aggregation event, we assessed the binding and interaction energy between a CPT-ss-BBR conjugate and an ICG molecule in the presence of excess $H_2O$ by 50 ns molecular dynamics (MD) simulations. For comparison, we also performed MD simulations of CPT-ss-BBR dimer and ICG dimer under the same conditions. As shown in Fig. 3, in the early stages of the simulation, the distance between the mass centers of the molecules decreased rapidly, which indicated that the molecules were clustering rapidly, but during the entire simulation process, the fluctuation of the CPT-ss-BBR/ICG complex was smaller, indicating a more stable aggregation. The binding free energy ($\Delta G_{total}$) of CPT-ss-BBR/ICG complex, CPT-ss-BBR dimer and ICG dimer was calculated by the MM-PBSA method (Table 1). The contribution to $\Delta G_{total}$ was divided into van der Waals ($\Delta E_{vdW}$) and electrostatic ($\Delta E_{elec}$) interaction energy, polar ($\Delta G_{polar}$) and nonpolar ($\Delta G_{nonpolar}$) solvation energy. As expected, the binding for CPT-ss-BBR/ICG complex was mainly governed by electrostatic interactions with $\Delta E_{elec}$ (–69.823 ± 5.699 kJ/mol), which largely cames from the attraction of positively charged CPT-ss-BBR and negatively charged ICG. A large part of the $\Delta G_{total}$ was also attributed to van der Waals interaction energy with $\Delta E_{vdW}$ (–53.362 ± 3.159 kJ/mol), which in view of the molecular structure, might indicate the existence of hydrophobic and π-π stacking interactions between molecules. The $\Delta G_{nonpolar}$ value (–6.719 ± 0.550 kJ/mol) was favorably for the complex, while $\Delta G_{polar}$ value (45.860 ± 3.847 kJ/mol) announced an unfavorable binding. The average value of $\Delta G_{total}$ of CPT-ss-BBR/ICG complex was found to be –84.044 ± 5.561 kJ/mol, lower than CPT-ss-BBR dimer (–31.006 ± 3.887 kJ/mol) and ICG dimer (–32.157 ± 1.839 kJ/mol), suggesting a more favorable binding for CPT-ss-BBR/ICG complex.

**Figure 3**

**Fig. 3.** Distances of centers of mass between monomers for CPT-ss-BBR/ICG complex, CPT-ss-BBR dimer and ICG dimer over time.

**Table 1.** The binding free energy (kJ/mol) and its components gained from the MM-PBSA calculations for CPT-ss-BBR/ICG complex, CPT-ss-BBR dimer and ICG dimer.

**Table 1**

As is well-known, electrostatic potential (ESP) as a reflection of electron density, affords a visual representation of the chemically or physically active sites.[45] In-depth investigation of ESP for the supramolecular assembly systems will be helpful for understanding the significant intermolecular interactions. In this work, ESP analysis was performed to qualitatively examine the active sites of the reaction involved in the construction of CPT-ss-BBR/ICG complex. The ESPs of CPT-ss-BBR and ICG were mapped onto their electron densities in Fig. 4. Results showed that the CPT-ss-BBR mainly exhibited positive charge, especially the BBR fragment. ICG as a whole was mainly negatively charged and concentrated on sulfonic groups. It could be predicted and had been confirmed that the electropositive BBR area of CPT-ss-BBR had an attraction for the electronegative sulfonic group of ICG during formation of the CPT-ss-BBR/ICG complex. However, the dimerization of positively-charged CPT-ss-BBR or negatively-charged ICG resulted in itself more positive (deeper blue) or negative (deeper red), which made the dimer less stable than the CPT-ss-BBR/ICG complex (a light color).

To further investigate the spontaneous process, we carried out a more long-time MD simulation (100 ns) on 10 molecules with the initial 1:1 molar ratio of CPT-ss-BBR to ICG. As depicted the snapshots of aggregation in Fig. 5, after a short simulation, five CPT-ss-BBR conjugates and five ICG molecules co-assemblied and formed well-organized clusters. The solvent accessible surface areas (SASA) of CPT-ss-BBR/ICG cluster, CPT-ss-BBR, ICG, CPT fraction and BBR fraction was shown in Fig. 6. Aggregation occurred during simulation as indicated by the SASA of CPT-ss-BBR/ICG cluster (blue curve) at 0 ns dropping from 118 to 52 nm$^2$ by 100 ns. The SASA of CPT-ss-BBR (black curve) and ICG (red curve) also partially declined throughout simulations. The CPT fraction (purple curve) had dropped slightly over this time frame, whereas the BBR fraction (green curve) had hardly changed, which indicated that BBR fraction remained similarly solvated during the process, and the CPT fraction was more likely to be inserted into the cluster.

**Figure 4**

**Fig. 4.** ESPs mapped on electron total density with an isovalue 0.001 a.u. The colors range from -0.18 a.u. shown in red to 0.18 a.u. in blue for CPT-ss-BBR, ICG, CPT-ss-BBR/ICG complex, CPT-ss-BBR dimer, ICG dimer.

Figure 5

**Fig. 5.** The supramolecular assembly process of CPT-ss-BBR conjugate with ICG in water by MD simulations. ICG is represented by pink, while CPT fragment and BBR fragment are yellow and blue, respectively. Water molecules and counterions are omitted for clarity.

Figure 6

**Fig. 6**. The solvent accessible surface areas of CPT-ss-BBR/ICG cluster (blue curve), CPT-ss-BBR (black curve), ICG (red curve), CPT fraction (purple curve) and BBR fraction (green curve).

### *3.4. In vitro photothermal effect of CPT-ss-BBR/ICG NPs*

To evaluate *in vitro* photothermal effects of CPT-ss-BBR/ICG NPs, the nanodrugs, ICG and PBS (control group) were irradiated with the most widely used NIR laser and the temperature change was monitored over time. As shown in Fig. 7A and B, the photothermal conversion performance of the CPT-ss-BBR/ICG NPs was basically consistent with the ICG aqueous solution. The increase value in temperature of nanodrugs changed from 19 to 24 $^{o}$C, when the concentration of ICG from CPT-ss-BBR/ICG NPs was 25 to 50 μM under the same laser irradiation (808 nm, 1 W/cm$^2$) for 5 min. In contrast, no obvious temperature change was detected in the control group ($\Delta T<5$ °C) at the same condition. Meanwhile, the increase value in temperature of nanodrugs changed from 24 to 28 $^{o}$C with the increase of power from 1 to 2 W/cm$^2$, which showed 47% higher photothermal effect than that under the conditions of ICG = 25 μM and 1 W/cm$^2$. These results indicated that the CPT-ss-BBR/ICG NPs held a good light-to-heat conversion effect, which was both concentration-dependent and laser-power-dependent and deserved further biomedical research in photothermal treatment.

Figure 7

**Fig. 7.** *In vitro* photothermal effect of CPT-ss-BBR/ICG NPs. (A) Infrared thermographic images with same ICG concentrations (25 μM) and PBS upon laser irradiation (808 nm, 1 W/cm$^2$) for different times. (B) Temperature variation curves of CPT-ss-BBR/ICG NPs and free ICG under different power intensities (808 nm, 1 or 2 W/cm$^2$) and different ICG concentrations.

### *3.5. In vitro drug release of CPT-ss-BBR/ICG NPs*

When normal cells become carcinogenic, the mitochondria become dysfunctional and express a higher level of GSH, which is enough to cleave the disulfide bond and disassembly the nanodrugs.[18] In addition, weak intermolecular interaction can be also destroyed by NIR irradiation and acid condition.[46] The release profiles of CPT and BBR-OH from CPT-ss-BBR/ICG NPs were measured using a typical dialysis method in the simulated physiological condition (pH = 5.6, 7.4 with 20 μM GSH) at body temperature for 72 h. Here, the accumulative amount of BBR-OH (**compound 3**) and CPT leaked out from our prepared nanodrugs was studied because BBR-OH and CPT might be the main form from NPs. As shown in Fig. 8A and B, CPT-ss-BBR/ICG NPs obviously exhibited GSH-responsive drug release behaviors, and the process could be accelerated by acid pH and NIR irradiation. Notably, upon the treatment of laser irradiation, 20 μM GSH and pH = 5.6, 80~85% of BBR-OH and CPT were released from CPT-ss-BBR/ICG NPs. The BBR-OH and CPT were released 50~60% within 10 h. Subsequently, BBR-OH and CPT continued to be released as the time went by. In contrast, only a few of BBR-OH and CPT were released from CPT-ss-BBR/ICG NPs in the control group. These release results indicated that such NIR/GSH/acid-sensitive drug release feature might allow the CPT-ss-BBR/ICG NPs to have a long-acting synergistic chemo-photothermal therapy effect.

**Figure 8**

**Fig. 8**. *In vitro* cumulative release of BBR-OH (A) or CPT (B) from CPT-ss-BBR/ICG NPs at various environment.

### *3.6. In vitro chemo-PTT therapy of CPT-ss-BBR/ICG NPs*

The *in vitro* synergistic chemo-PTT effect of CPT-ss-BBR/ICG NPs was further assessed by MTT assay. As observed from Fig. 9 and Table 2, at the same dosage, the chemo-PTT of the CPT-ss-BBR/ICG NPs was obviously better than that of single CPT chemotherapy. In detail, in the absence of laser, the inhibitory effect of the CPT-ss-BBR/ICG NPs on A549 cells was positively related to the concentration of the drug and the time of administration. Although the nanodrugs' inhibitory activity was less than that of CPT after 24 h of administration, the its anticancer activity of ($IC_{50}$ = 0.93 and 0.48 μM, respectively) was comparable to that of CPT after 48 h ($IC_{50}$ = 0.90 μM) or 72 h ($IC_{50}$ = 0.43 μM) incubation, with a much lower $IC_{50}$ than free CPT-ss-BBR ($IC_{50}$ = 1.16 and 0.63 μM, respectively). These results might be ascribed to mitochondrial-targeted drug delivery and release over time. The photothermal performance of CPT-ss-BBR/ICG NPs was evaluated under the 808 nm laser irradiation (5 min, 1 W/cm$^2$). After laser irradiation, CPT-ss-BBR/ICG NPs displayed prominently higher therapeutic outcomes as compared to the free CPT. Especially, the inhibitory activity of nanodrugs ($IC_{50}$ = 0.21 μM) was twice than CPT ($IC_{50}$ = 0.43 μM) after 72 h incubation, which might be attributed to irreversible photothermal damage. Therefore, mitochondrial-targeted combinational therapy had the potential to address cancer recurrence and metastasis caused by incomplete chemotherapy effects. The anti-tumor efficacy was further evaluated with Calcein-AM and PI assays, almost all the cells were dead after treatment with CPT-ss-BBR/ICG NPs (laser irradiation) (Fig. 10), again demonstrating the potent chemo-PTT effect of nanodrugs against A549 cells.

**Figure 9**

**Fig. 9**. *In vitro* anticancer activity of co-assembled CPT-ss-BBR/ICG NPs (with or without laser irradiation), CPT-ss-BBR, CPT, BBR-OH, ICG (with or without laser irradiation) against A549 cells for 24 h (A), 48 h (B) and 72 h (C). Statistical signifcance: $^{**}p < .01$, $^{***}p < .005$.

**Table 2**. $IC_{50}$ values of co-assembled CPT-ss-BBR/ICG NPs (with or without laser irradiation), CPT-ss-BBR, CPT, BBR-OH, ICG (with or without laser irradiation) against A549 cells at different times.

**Table 2**

**Figure 10**

**Fig. 10.** Live/dead fluorescence staining of A549 cell treated with PBS (control), CPT-ss-BBR/ICG NPs (with or without laser irradiation), CPT-ss-BBR, CPT, BBR-OH, ICG (with or without laser irradiation) (Scale bars: 80 μm). Green represents the live cells and red indicates the dead cells.

### *3.7. Apoptosis-inducing effect in vitro by CPT-ss-BBR/ICG NPs*

Additionally, to further demonstrate induced apoptosis of CPT-ss-BBR/ICG NPs, A549 cells were treated with PBS (control), CPT-ss-BBR/ICG NPs (with or without laser irradiation), CPT-ss-BBR, CPT, BBR-OH, ICG (with or without laser irradiation). After 24 h of incubation, the cell apoptosis was analyzed by Annexin V-FITC/PI staining. As depicted in Fig. 11, in the presence of irradiation, the total ratio of the early apoptosis and late apoptosis induced by nanodrugs was ~85%, which was extremely higher than any other experimental groups, especially twice that of the CPT group, which revealed a cellular synergistic chemo-photothermal effect of CPT-ss-BBR/ICG NPs.

**Figure 11**

**Fig. 11**. Apoptosis ratio of A549 cells detected by flow cytometry induced by PBS (control), CPT-ss-BBR/ICG NPs (with or without laser irradiation), CPT-ss-BBR, CPT, BBR-OH, ICG (with or without laser irradiation).

### *3.8. Mitochondria targeting of CPT-ss-BBR/ICG NPs*

To test the mitochondria targeted property of CPT-ss-BBR/ICG NPs, the commercial dye, Mitotracker Red, was employed for staining the mitochondria in A549 cells for the detection. After 45 or 90 minutes of nanodrugs incubation and 25 minutes of dye treatment, we monitored the intracellular mitochondrial localization by CLSM. The green fluorescence of berberine overlaped with the red fluorescence of the dye to produce yellow fluorescence. The degree of mitochondrial colocalization was represented by the Pearson's correlation coefficient. As found from Fig. 12, all of BBR-OH, CPT-ss-BBR and CPT-ss-BBR/ICG NPs (for 45 or 90 min) could co-localize mitochondria with dyes in A549 cells and the Pearson's correlation coefficient was 0.973, 0.977, 0.912 and 0.965, respectively. Moreover, over time, it became apparent that the co-localized fluorescence intensity of the nanodrugs increased. These results indicated that the CPT-ss-BBR/ICG NPs had excellent mitochondrial targeting property and time-dependent uptake characteristics.

**Figure 12**

**Fig. 12**. Mitochondria targeting of the BBR-OH, CPT-ss-BBR and CPT-ss-BBR/ICG NPs in A549 cells detected by CLSM (Scale bars: 120 μm).

### *3.9. Mitochondrial membrane potential assay*

The energy obtained from the double-membrane-structured mitochondrial respiration forces the protons in the mitochondrial matrix to pass through the inner membrane to form a mitochondrial membrane potential (ΔΨ), which plays an important role in regulating cellular processes such as cell apoptosis pathway and release of ROS.[47] JC-1 was a lipophilic cationic dye, which could selectively accumulate into cancer cell mitochondria in the form of J-aggregates and emitted red fluorescence, but the loss of ΔΨ led to the dye existing as a monomer and emitted green light. To evaluate the mitochondrial damage before and after the treatment with nanodrugs, the JC-1 dye was employed for assessing the changes of ΔΨ. Our results (Fig. 13 and 14) found that the ΔΨ of all experimental groups had a significant loss when compared with the control group. Especially upon the treatment of NIR irradiation, CPT-ss-BBR/ICG NPs decreased ΔΨ by approximately 40%, which was significantly better than CPT.

**Figure 13**

**Fig. 13**. Variations of mitochondrial membrane potential in A549 cells detected by flow cytometry induced by PBS (control), CPT-ss-BBR/ICG NPs (with or without laser irradiation), CPT-ss-BBR, CPT, BBR-OH, ICG (with or without laser irradiation).

**Figure 14**

**Fig. 14**. The CLSM results of mitochondrial membrane potential of A549 cells treated with PBS (control), CPT-ss-BBR/ICG NPs (with or without laser irradiation), CPT-ss-BBR, CPT, BBR-OH, ICG (with or without laser irradiation) (Scale bars: 100 μm).

### *3.10 Intracellular ROS production*

ROS is responsible for holding intracellular redox homeostasis. High levels of ROS in cancer cells will attack biological macromolecules, such as proteins, nucleic acids, phospholipids, etc., which will cause irreversible damage to the physiological functions of the cells and eventually result in cell death.[48] 2,7-Dichlorofluorescein diacetate (DCFH-DA) is a probe that has no fluorescence outside the cell and can freely pass through the cell membrane. Once it enters the cell, it will be oxidized by active oxygen to 2,7-dichlorofluorescein (DCF) with green fluorescence. The DCFH-DA is used for detecting intracellular ROS level. Fig. 15 and 16 suggested that ROS generation was greatly elevated when CPT-ss-BBR/ICG NPs was exposed to 808 nm laser and the its photoactivity was superior to control groups and CPT.

**Figure 15**

**Fig. 15**. Intracellular ROS production measured by flow cytometry in A549 cells induced by PBS

(control), CPT-ss-BBR/ICG NPs (with or without laser irradiation), CPT-ss-BBR, CPT, BBR-OH, ICG (with or without laser irradiation).

**Figure 16**

**Fig. 16**. The CLSM results of intracellular ROS level of A549 cells induced by PBS (control), CPT-ss-BBR/ICG NPs (with or without laser irradiation), CPT-ss-BBR, CPT, BBR-OH, ICG (with or without laser irradiation) (Scale bars: 100 μm).

## 4. Discussion

Mitochondria act as energy factories in cells, indirectly or directly controlling cell growth, differentiation and metabolism of substances and affecting various physiological functions. Therefore, the delivery of drugs directly to the mitochondria has the potential to increase the uptake of drugs and cause irreversible damage to them, thereby improving the therapeutic effect. In this work, we had made full use of the advantages of berberine (BBR), camptothecin (CPT) and indocyanine green (ICG), and successfully constructed mitochondria-targeted stimuli-responsive supramolecular self-assembled nanodrugs (CPT-ss-BBR/ICG NPs) that could achieve chemotherapy and photothermal combination therapy.

The prepared nanodrugs showed a regular spherical shape and appeared very uniform in size (approximately 168 nm by DLS) and could maintain the size for a long time in the absence of external stimuli. MD simulations revealed that the binding between CPT-ss-BBR and ICG was mainly governed by electrostatic interactions, which largely cames from the attraction of positively charged CPT-ss-BBR and negatively charged ICG. The *in vitro* photothermal effects indicated that the temperature changes of CPT-ss-BBR/ICG NPs with good photothermal properties were both concentration-dependent and laser-power-dependent and deserved further biomedical research in photothermal treatment. Furthermore, CPT-ss-BBR/ICG NPs obviously exhibited GSH-responsive release behaviors of BBR-OH and CPT, and the process could be accelerated by acid pH and NIR irradiation. Such triply sensitive drug release feature might allow the CPT-ss-BBR/ICG NPs to have a long-acting synergistic chemo-photothermal therapy effect. Due to the presence of BBR moiety, the CPT-ss-BBR/ICG NPs had excellent mitochondrial targeting property and time-dependent uptake characteristics. Based on above advantages and as expected, the *in vitro* synergistic chemo-PTT effect suggested that after laser irradiation, CPT-ss-BBR/ICG NPs displayed prominently higher therapeutic outcomes as compared to the free CPT. Therefore, mitochondrial-targeted combinational therapy had the potential to address cancer recurrence and metastasis caused by incomplete chemotherapy effects.

Additionally, in the presence of irradiation, the total ratio of the apoptosis induced by nanodrugs was ~85%, which was twice higher than free CPT. To further investigate the possible mechanisms of CPT-ss-BBR/ICG NPs, we conducted mitochondrial membrane potential and reactive oxygen studies. $\Delta\Psi$ of all experimental groups had a significant loss when compared with the control group. Especially upon the treatment of NIR irradiation, CPT-ss-BBR/ICG NPs decreased ΔΨ by approximately 40%, which was significantly better than CPT. ROS generation was greatly elevated when CPT-ss-BBR/ICG NPs was exposed to 808 nm laser and the its photoactivity was superior to control groups and CPT.

## 5. Conclusion

In summary, we successfully fabricated a mitochondria-targeting nanodrugs (CPT-ss-BBR/ICG NPs) constructed by a GSH-reduced conjugate and a photosensitizer for combined chemical and photothermal therapy of tumor. In our strategy, TEM and DLS suggested that the obtained nanodrugs possessed an excellent stability in physiological environment and a suitbale particle size with uniform monodispersity. The computational simulations elucidated that the spontaneous binding driven forces of the co-assembly nanosystem were stemmed from hydrophobic, π-π stacking and especially, electrostatic interactions of anions and cations, which provided helpful insights into the reasonable construction of functional supramolecular assemblies. The *in vitro* drug release assay announced that the irradiation presence, acid condition and high concentration of GSH were capable of triggering the rapid disassembly of nanodrugs and accelerated drug release. Moreover, CPT-ss-BBR/ICG NPs could specifically target mitochondria from cancer cells due to its intrinsic lipocationic properties and induce rapid photothermal conversion, high level of ROS and great loss of ΔΨ upon the treatment of NIR irradiation. Consequently, the nanodrugs exerted powerful inhibition against A549 cells in the presence of light when compared to CPT. It could be concluded that CPT-ss-BBR/ICG NPs were prospective carrier-free nanoarchitectures for improving the efficacy of combined chemical and photothermal therapy of tumor.

## Acknowledgement

The authors gratefully acknowledge Xin Jiang from Shandong Normal University and Dr. Defang Ouyang from University of Macau for helping with paper’s format revision and quantum chemistry calculations and the financial support for this research from the National Natural Science Foundation of China (Grant No.: 21978047, 21776046), the Fundamental Research Funds for the Central Universities (Grant No.: 2242019K40145, 2242020K40033).

## References

[1] J. Shi, P.W. Kantoff, R. Wooster, O.C. Farokhzad, Cancer nanomedicine: Progress, challenges and opportunities, Nat. Rev. Cancer 17 (2017) 20–37.

[2] R. van der Meel, E. Sulheim, Y. Shi, F. Kiessling, W.J.M. Mulder, T. Lammers, Smart cancer nanomedicine, Nat. Nanotechnol. 14 (2019) 1007–1017.

[3] Y. Cheng, Y.H. Ji, RGD-modified polymer and liposome nanovehicles: Recent research progress for drug delivery in cancer therapeutics, Eur. J. Pharm. Sci. 128 (2019) 8–17.

[4] S. Walker, S. Busatto, A. Pham, M. Tian, A. Suh, K. Carson, A. Quintero, M. Lafrence, H. Malik, M.X. Santana, J. Wolfram, Extracellular vesicle-based drug delivery systems for cancer treatment, Theranostics 9 (2019) 8001–8017.

[5] M.A. Grimaudo, A. Concheiro, C. Alvarez-Lorenzo, Nanogels for regenerative medicine, J. Control. Release 313 (2019) 148–160.

[6] D. Wang, T. Zhao, X. Zhu, D. Yan, W. Wang, Bioapplications of hyperbranched polymers, Chem. Soc. Rev. 44 (2015) 4023–4071.

[7] K. Hörmann, A. Zimmer, Drug delivery and drug targeting with parenteral lipid nanoemulsions — A review, J. Control. Release 223 (2016) 85–98.

[8] Z. Zhang, Y.H. Ji, Mesoporous manganese dioxide coated gold nanorods as a multiresponsive nanoplatform for drug delivery, Ind. Eng. Chem. Res. 58 (2019) 2991–2999.

[9] D. Wang, C. Yu, L. Xu, L. Shi, G. Tong, J. Wu, H. Liu, D. Yan, X. Zhu, Nucleoside analogue-based supramolecular nanodrugs driven by molecular recognition for synergistic cancer therapy, J. Am. Chem. Soc. 140 (2018) 8797–8806.

[10] Y. Xu, Y. Huang, X. Zhang, W. Lu, J. Yu, S. Liu, Carrier-free Janus nano-prodrug based on camptothecin and gemcitabine: reduction-triggered drug release and synergistic in vitro antiproliferative effect in multiple cancer cells, Int. J. Pharm. 550 (2018) 45–56.

[11] F. Peng, M.I. Setyawati, J.K. Tee, X. Ding, J. Wang, M.E. Nga, H.K. Ho, D.T. Leong, Nanoparticles promote in vivo breast cancer cell intravasation and extravasation by inducing endothelial leakiness, Nat. Nanotechnol. 14 (2019) 279–286.

[12] M. Elsabahy, K.L. Wooley, Data mining as a guide for the construction of cross-linked nanoparticles with low immunotoxicity *via* control of polymer chemistry and supramolecular assembly, Acc. Chem. Res. 48 (2015) 1620–1630.

[13] S.F. Hansen, A. Lennquist, Carbon nanotubes added to the SIN list as a nanomaterial of very high concern, Nat. Nanotechnol. 15 (2020) 3–4.

[14] X. Wang, X. Cheng, L. He, X.L. Zeng, Y. Zheng, R.P. Tang, Self-assembled indomethacin dimer nanoparticles loaded with doxorubicin for combination therapy in resistant breast cancer, ACS Appl. Mater. Interfaces 11 (2019) 28597–28609.

[15] Q. Zou, M. Abbas, L. Zhao, S. Li, G. Shen, X. Yan, Biological photothermal nanodots based on self-assembly of peptide−porphyrin conjugates for antitumor therapy, J. Am. Chem. Soc. 139 (2017) 1921–1927.

[16] Z. Guo, L. Lin, K. Hao, D. Wang, F. Liu, P. Sun, H. Yu, Z. Tang, M. Chen, H. Tian, X. Chen, Helix self-assembly behavior of amino acid-modified camptothecin prodrugs and its antitumor effect, ACS Appl. Mater. Interfaces 12 (2020) 7466−7476.

[17] I. Noh, D. Lee, H. Kim, C.U. Jeong, Y. Lee, J.O. Ahn, H. Hyun, J.H. Park, Y.C. Kim, Enhanced photodynamic cancer treatment by mitochondria-targeting and brominated near-infrared fluorophores, Adv. Sci. 5 (2018) 1700481.

[18] Y. Wang, T. Zhang, C. Hou, M. Zu, Y. Lu, X. Ma, D. Jia, P. Xue, Y. Kang, Z. Xu, Mitochondria-specific anticancer drug delivery based on reduction-activated polyprodrug for enhancing the therapeutic effect of breast cancer chemotherapy, ACS Appl. Mater. Interfaces 11 (2019) 29330–29340.

[19] H. Chen, J. Wang, X. Feng, M. Zhu, S. Hoffmann, A. Hsu, K. Qian, D. Huang, F. Zhao, W. Liu, H. Zhang, Z. Cheng, Mitochondria-targeting fluorescent molecules for high efficiency cancer growth inhibition and imaging, Chem. Sci. 10 (2019) 7946–7951.

[20] Y. Geng, Y. Zhong, Q. Zhou, S. Chen, Y. Piao, W. Yin, H. Lu, Y. Shen, A neutral water-soluble mitochondria-targeting polymer, Chem. Commun. 55 (2019) 10015–10018.

[21] X. Feng, A. Sureda, S. Jafari, Z. Memarian, D. Tewari, G. Annunziata, L. Barrea, S.T.S. Hassan, K. Šmejkal, M. Malanik, A. Sychrová, D. Barreca, L. Ziberna, M.F. Mahomoodally, G. Zengin, S. Xu, S.M. Nabavi, A.Z. Shen, Berberine in cardiovascular and metabolic diseases: From mechanisms to therapeutics, Theranostics 9 (2019) 1923–1951.

[22] H. Li, C. Fan, H. Lu, C. Feng, P. He, X. Yang, C. Xiang, J. Zuo, W. Tang, Protective role of berberine on ulcerative colitis through modulating enteric glial cells-intestinal epithelial cells-immune cells interactions, Acta Pharm. Sin. B 10 (2020) 447–461.

[23] L. Han, W. Sheng, X. Li, A. Sik, H. Lin, K. Liu, L. Wang, Novel carbohydrate modified berberine derivatives: Synthesis and *in vitro* anti-diabetic investigation, Med. Chem. Commun. 10 (2019) 598–605.

[24] W.J. Kong, C. Vernieri, M. Foiani, J.D. Jiang, Berberine in the treatment of metabolism-related chronic diseases: a drug cloud (dCloud) effect to target multifactorial disorders, Pharmacol. Ther. (2020) doi.org/10.1016/j.pharmthera.2020.107496.

[25] S. Fu, Y. Xie, J. Tuo, Y. Wang, W. Zhu, S. Wu, G. Yan, H. Hu, Discovery of mitochondria-targeting berberine derivatives as the inhibitors of proliferation, invasion and migration against rat C6 and human U87 glioma cells, Med. Chem. Commun. 6 (2015) 164–173.

[26] J. Tuo, Y. Xie, J. Song, Y. Chen, Q. Guo, X. Liu, X. Ni, D. Xu, H. Huang, S. Yin, W. Zhu, J. Wu, H. Hu, Development of a novel berberine-mediated mitochondriatargeting nano-platform for drug-resistant cancer therapy, J. Mater. Chem. B 4 (2016) 6856–6864.

[27] R. An, Z. Gu, H. Sun, Y. Hu, R. Yan, D. Ye, H. Liu, Self-assembly of fluorescent dehydroberberine enhances mitochondria-dependent antitumor efficacy, Chem. Eur. J. 24 (2018) 9812–9819.

[28] J. Song, C. Lin, X. Yang, Y. Xie, P. Hu, H. Li, W. Zhu, H. Hu, Mitochondrial targeting nanodrugs self-assembled from 9-O-octadecyl substituted berberine derivative for cancer treatment by inducing mitochondrial apoptosis pathways, J. Control. Release 294 (2019) 27–42.

[29] C.V. Diogo, N.G. Machado, I.A. Barbosa, T.L. Serafim, A. Burgeiro, P.J. Oliveira, Berberine as a promising safe anti-cancer agent-is there a role for mitochondria? Curr. Drug Targets 12 (2011) 850–859.

[30] Y. Cheng, Y.H. Ji, Mitochondria-targeting nanomedicine self-assembled from GSH-responsive paclitaxel-ss-berberine conjugate for synergetic cancer treatment with enhanced cytotoxicity, J. Control. Release 318 (2020) 38–49.

[31] P. Pan, J. Chen, X. Li, M. Li, H. Yu, J.J. Zhao, J. Ni, X. Wang, H. Sun, S. Tian, F. Zhu, F. Liu, Y. Huang, T. Hou, Structure-based drug design and identification of $H_2O$-soluble and low toxic hexacyclic camptothecin derivatives with improved efficacy in cancer and lethal inflammation models *in vivo*, J. Med. Chem. 61 (2018) 8613–8624.

[32] K. Mulholland, C. Wu, Computational study of anticancer drug resistance caused by 10 topisomerase I mutations, including 7 camptothecin analogs and lucanthone, J. Chem. Inf. Model. 56 (2016) 1872–1883.

[33] C.P. Liu, C.Y. Xie, J.X. Zhao, K.L. Ji, X.X. Lei, H. Sun, L.G. Lou, J.M. Yue, Dysoxylactam a: a macrocyclolipopeptide reverses p-glycoproteinmediated multidrug resistance in cancer cells, J. Am. Chem. Soc. 141 (2019) 6812−6816.

[34] W. Zhang, X. Hu, Q. Shen, D. Xing, Mitochondria-specific drug release and reactive oxygen species burst induced by polyprodrug nanoreactors can enhance chemotherapy, Nat. Commun. 10 (2019) 1704.

[35] T. Zhang, X. Ma, S. Bai, Y. Wang, X. Zhang, Y. Lu, F. Wen, P. Xue, Y. Kang, Z. Xu, Reactive oxygen species-activatable camptothecin polyprodrug based dextran enhances chemotherapy efficacy by damaging mitochondria, J. Mater. Chem. B 8 (2020) 1245–1255.

[36] N. Sen, B.B. Das, A. Ganguly, T. Mukherjee, G. Tripathi, S. Bandyopadhyay, S. Rakshit, T. Sen, H.K. Majumder, Camptothecin induced mitochondrial dysfunction leading to programmed cell death in unicellular hemoflagellate Leishmania donovani, Cell Death Differ. 11 (2004) 924–936.

[37] Z. Guo, X. Zhou, M. Xu, H. Tian, X. Chen, M. Chen, Dimeric camptothecin-loaded RGD-modified targeted cationic polypeptide-based micelles with high drug loading capacity and redox-responsive drug release capability, Biomater. Sci. 5 (2017) 2501–2510.

[38] W. Fan, B. Yung, P. Huang, X. Chen, Nanotechnology for multimodal synergistic cancer therapy, Chem. Rev. 117 (2017) 13566–13638.

[39] J. Beik, M. Khateri, Z. Khosravi, S.K. Kamrava, S. Kooranifar, H. Ghaznavi, A. Shakeri-Zadeh, Gold nanoparticles in combinatorial cancer therapy strategies, Coord. Chem. Rev. 387 (2019) 299–324.

[40] L.H. Fu, C. Qi, Y.R. Hu, J. Lin, P. Huang, Glucose oxidase-instructed multimodal synergistic cancer therapy, Adv. Mater. 31 (2019) 1808325.

[41] S.L. Gai, G.X. Yang, P.P. Yang, F. He, J. Lin, D.Y. Jin, B.G. Xing, Recent advances in functional nanomaterials for light–triggered cancer therapy, Nano Today 19 (2018) 146–187.

[42] Y.J. Liu, P. Bhattarai, Z.F. Dai, X.Y. Chen, Photothermal therapy and photoacoustic imaging *via* nanotheranostics in fighting cancer, Chem. Soc. Rev. 48 (2019) 2053–2108.

[43] M. Mravic, J.L. Thomaston, M. Tucker, P.E. Solomon, L. Liu, W.F. DeGrado, Packing of apolar side chains enables accurate design of highly stable membrane proteins, Science 363 (2019) 1418–1423.

[44] A.J. Pak, J.M.A. Grime, A. Yu, G.A. Voth, Off-Pathway assembly: a broad-spectrum mechanism of action for drugs that undermine controlled HIV-1 viral capsid formation, J. Am. Chem. Soc. 141 (2019) 10214–10224.

[45] X. Zhao, G. Zhu, L. Jiao, F. Yu, C. Xie, Formation and extractive desulfurization mechanisms of aromatic acid based deep eutectic solvents: an experimental and theoretical study, Chem. Eur. J. 24 (2018) 11021–11032.

[46] S. Ye, F. Wang, Z. Fan, Q. Zhu, H. Tian, Y. Zhang, B. Jiang, Z. Hou, Y. Li, G. Su, Light/pH-triggered biomimetic red blood cell membranes camouflaged small molecular drug assemblies for imaging-guided combinational chemo-photothermal therapy, ACS Appl. Mater. Interfaces 11 (2019) 15262−15275.

[47] V.L. Shailaja, V.S. Christina, C.D. Mohanapriya, P. Sneha, R.L. Sundaram, R. Magesh, C.G.P. Doss, K.M.E. Gnanambal, A natural anticancer pigment, Pheophytin a, from a seagrass acts as a high affinity human mitochondrial translocator protein (TSPO) ligand, in silico, to reduce mitochondrial membrane potential (Δψmit) in adenocarcinomic A549 cells, Phytomedicine 61 (2019) 152858.

[48] B. Yang, Y. Chen, J. Shi, Reactive oxygen species (ROS)-based nanomedicine, Chem. Rev. 119 (2019) 4881−4985.

**Table 1.** The binding free energy (kJ/mol) and its components gained from the MM-PBSA calculations for CPT-ss-BBR/ICG complex, CPT-ss-BBR dimer and ICG dimer.

| Contribution | CPT-ss-BBR/ICG complex | CPT-ss-BBR dimer | ICG dimer |
|---|---|---|---|
| $\Delta E_{vdw}$ | –53.362 ± [illegible].159 | –102.558 ± 8.487 | –90.877 ± 5.054 |
| $\Delta E_{elec}$ | –69.823 ± 5.699 | 26.402 ± 1.290 | 33.992 ± 1.343 |
| $\Delta G_{polar}$ | 45.860 ± 3.847 | 54.160 ± 4.055 | 34.506 ± 2.415 |
| $\Delta G_{nonpolar}$ | –6.719 ± 0.550 | –9.010 ± 0.745 | –9.778 ± 0.543 |
| $\Delta G_{total}$ | –84.044 ± 5.561 | –31.006 ± 3.887 | –32.157 ± 1.839 |

**Table 2**. $IC_{50}$ values of co-assembled CPT-ss-BBR/ICG NPs (with or without laser irradiation), CPT-ss-BBR, CPT, BBR-OH, ICG (with or without laser irradiation) against A549 cells at different times.

| Formulations | $IC_{50}$ (μM) | | |
|---|---|---|---|
| | 24 h | 48 h | 72 h |
| CPT-ss-BBR/ICG NPs | 5.48 ± 0.38 | 0.93 ± 0.12 | 0.48 ± 0.06 |
| CPT-ss-BBR/ICG NPs (with laser irradiation) | 3.06 ± 0.11 | 0.36 ± 0.11 | 0.21 ± 0.08 |

| | | | |
|---|---|---|---|
| CPT | 4.49 ± 0.34 | 0.90 ± 0.10 | 0.43 ± 0.10 |
| BBR-OH | 33.71 ± 1.79 | 21.12 ± 4.99 | 14.18 ± 3.72 |
| ICG | 134.30 ± 17.86 | 89.91 ± 12.46 | 72.72 ± 7.83 |
| ICG (with laser irradiation) | 13.65 ± 0.49 | 10.56 ± 3.25 | 6.86 ± 0.48 |
| CPT-ss-BBR | 5.93 ± 0.35 | 1.16 ± 0.30 | 0.63 ± 0.10 |

CRediT author statement:

**Yu Cheng**: Writing - Original Draft, Methodology, Data Curation, Formal analysis

**Yuanhui Ji** *: Writing - Review & Editing, Conceptualization, Supervision, Resources

**Jiwei Tong**: Writing - Original Draft, Data Curation

# Triply stimuli-responsive mitochondria-targeting supramolecular nanodrugs co-assembled mainly by electrostatic attraction for enhanced chemo-photothermal combination therapy

Yu Cheng, Yuanhui Ji*, Jiwei Tong

*Jiangsu Province Hi-Tech Key Laboratory for Biomedical Research, School of Chemistry and Chemical Engineering, Southeast University, Nanjing, 211189, P.R. China.*

* Corresponding author: Tel: +86-13951907361; Email: yuanhui.ji@seu.edu.cn; yuanhuijinj@163.com.

The prepared mitochondria-targeting NIR/GSH/pH-sensitive CPT-ss-BBR/ICG NPs were mainly driven by electrostatic attraction. The excellent therapy effect of nanodrugs on A549 cells might be attributed to triply stimuli-responsive rapid disassembly, preferable accumulation into mitochondria and combined chemotherapy and photothermal therapy, all of which directly rendered the notable loss of mitochondria membrane potential, high level of reactive oxygen species in cancer cells, accelerated the apoptosis of cancer cells and repressed the growth of tumors.

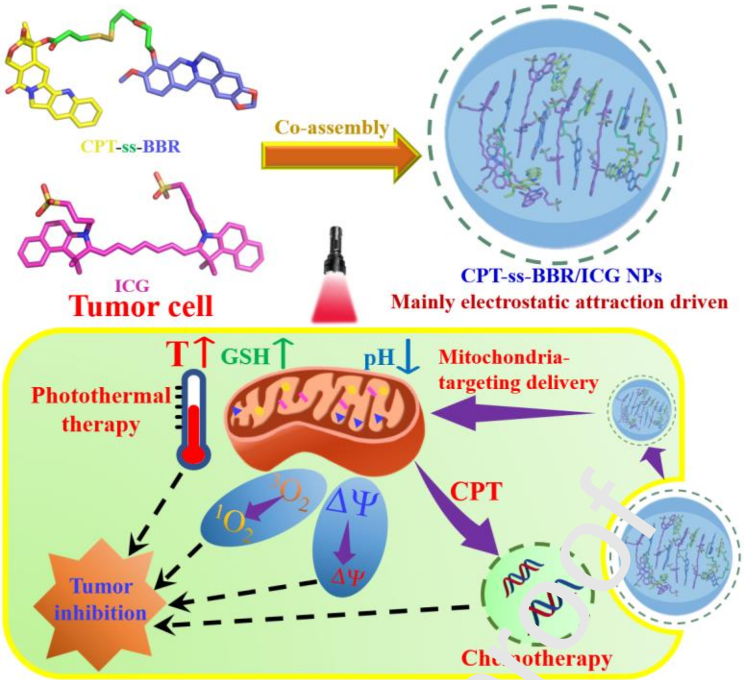

- New mitochondria-targeting CPT-ss-BBR/ICG NPs were developed.
- Prepared nanodrugs showed NIR/GSH/pH-sensitive drug release characteristics.
- Computer simulation studies rationalized the co-assembly process of CPT-ss-BBR and ICG.
- CPT-ss-BBR/ICG NPs exhibited better anticancer activity by acting on mitochondria.

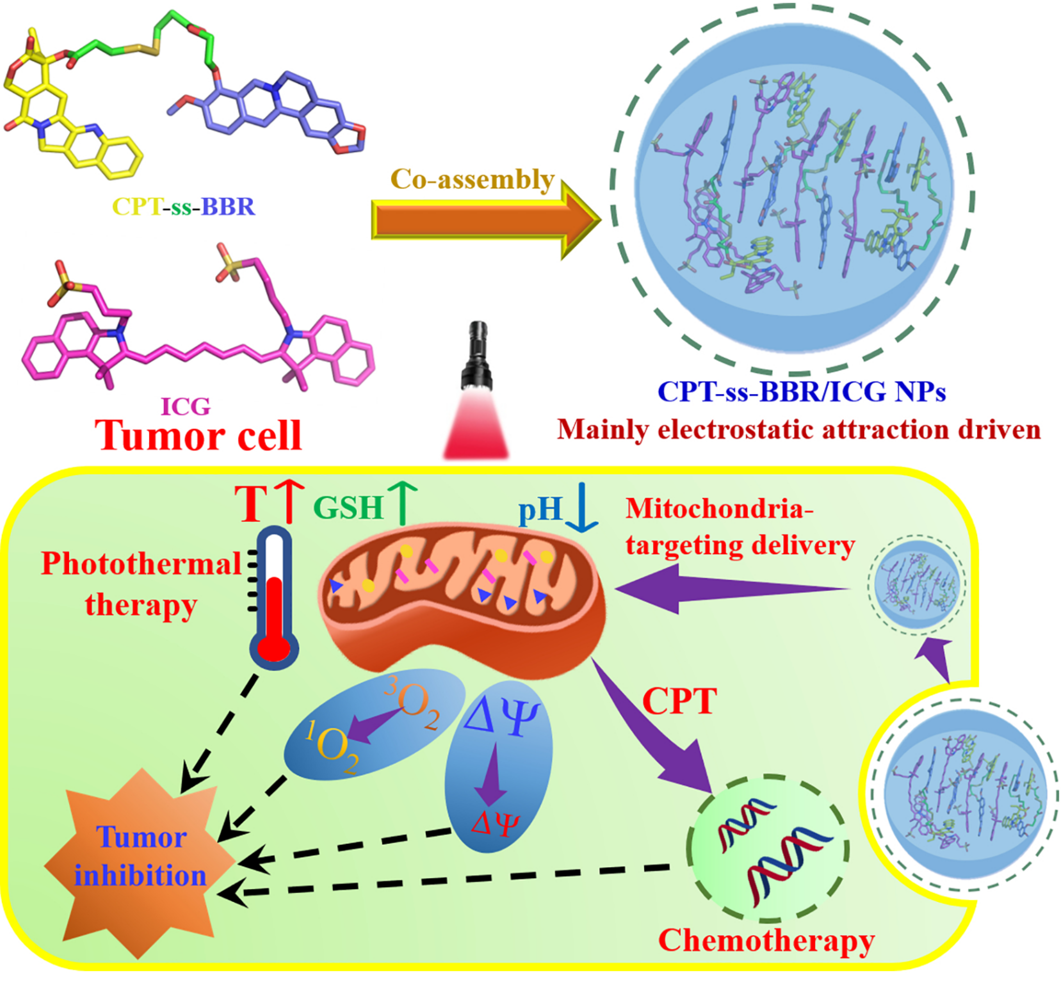
CPT-ss-BBR
ICG
Co-assembly
CPT-ss-BBR/ICG NPs
Mainly electrostatic attraction driven
Tumor cell
T↑
GSH↑
pH↓
Mitochondria-targeting delivery
Photothermal therapy
$^3O_2$
$^1O_2$
ΔΨ
ΔΨ
CPT
Tumor inhibition
Chemotherapy

Figure 1

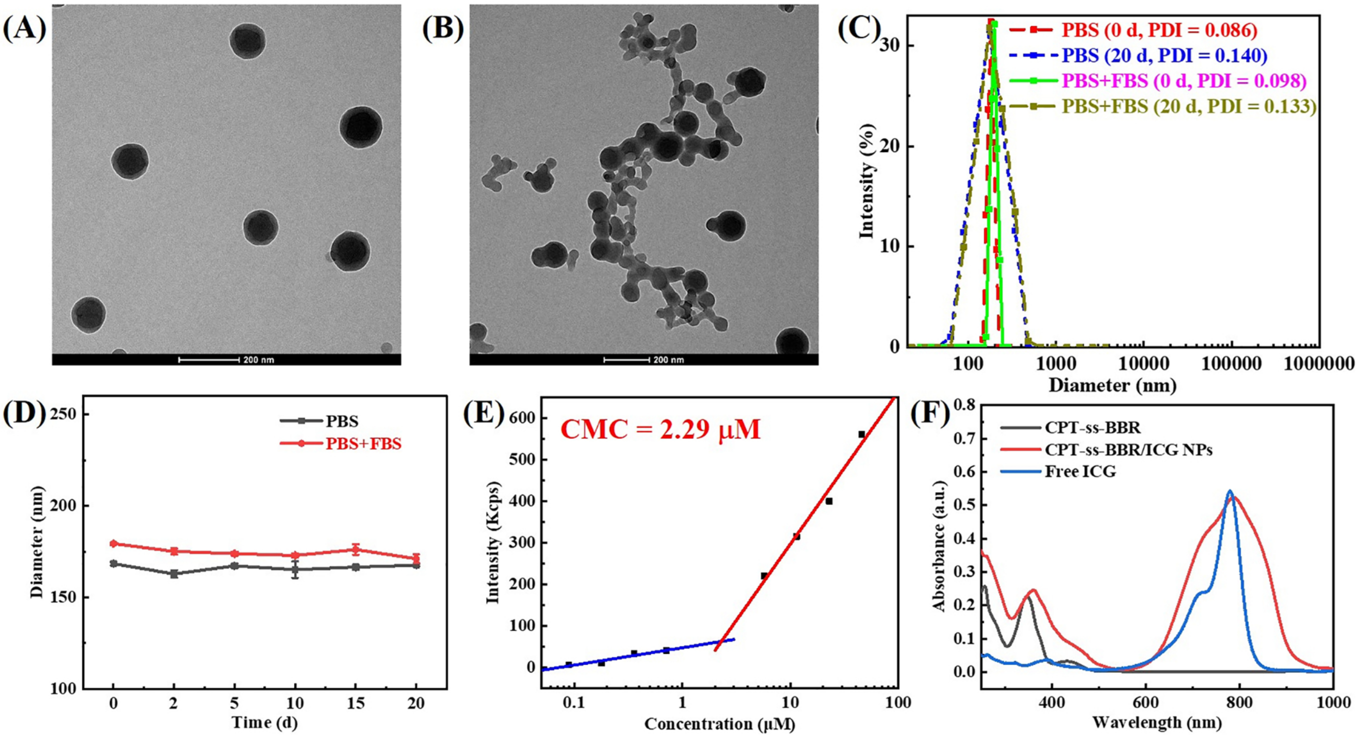
(A)
200 nm
(B)
200 nm
(C)
PBS (0 d, PDI = 0.086)
PBS (20 d, PDI = 0.140)
PBS+FBS (0 d, PDI = 0.098)
PBS+FBS (20 d, PDI = 0.133)
Intensity (%)
0
10
20
30
100
1000
10000
100000
1000000
Diameter (nm)
(D)
PBS
PBS+FBS
Diameter (nm)
100
150
200
250
0
2
5
10
15
20
Time (d)
(E)
CMC = 2.29 μM
Intensity (Kcps)
0
100
200
300
400
500
600
0.1
1
10
100
Concentration (μM)
(F)
CPT-ss-BBR
CPT-ss-BBR/ICG NPs
Free ICG
Absorbance (a.u.)
0.0
0.1
0.2
0.3
0.4
0.5
0.6
0.7
0.8
400
600
800
1000
Wavelength (nm)

Figure 2

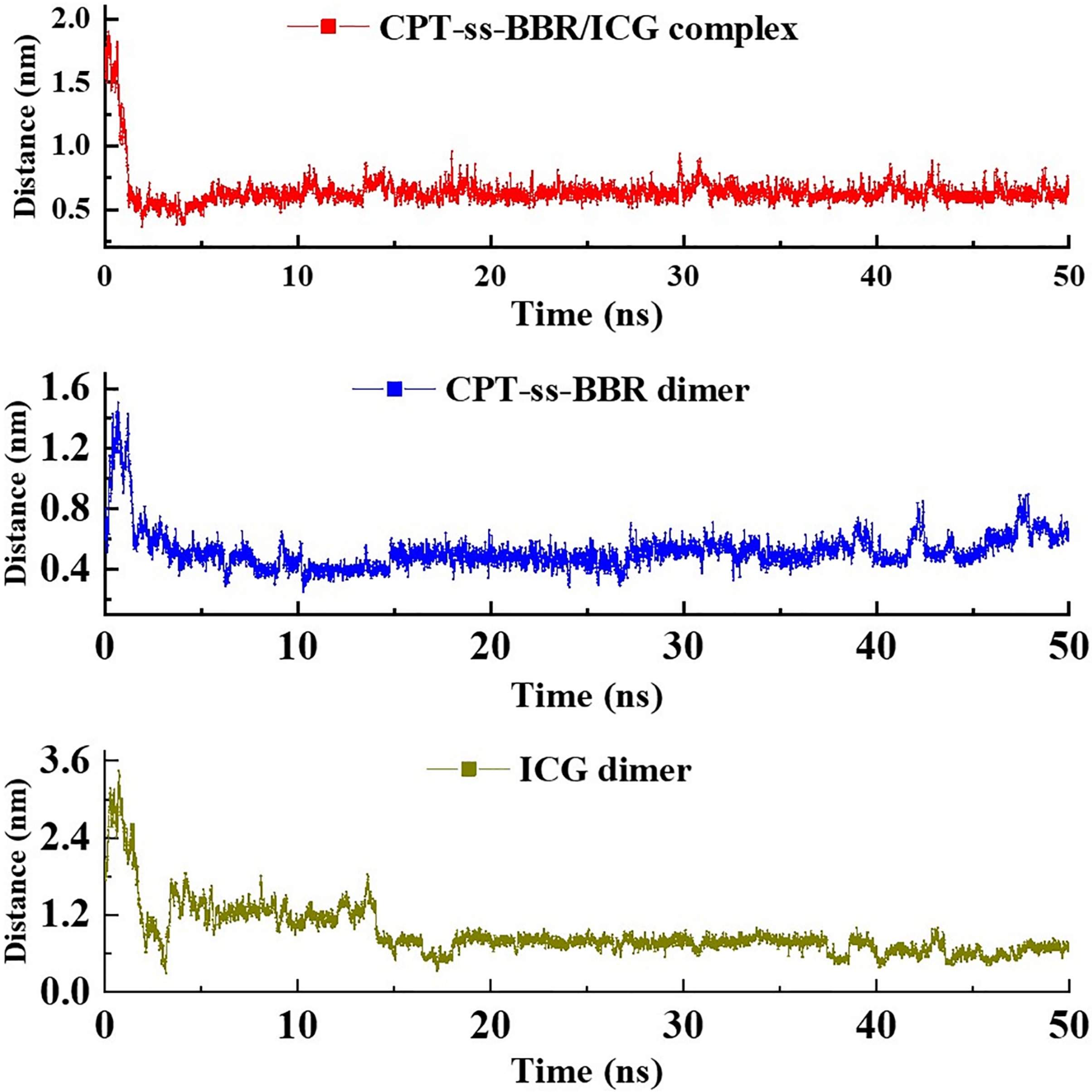
CPT-ss-BBR/ICG complex
Distance (nm)
2.0
1.5
1.0
0.5
0
10
20
30
40
50
Time (ns)
CPT-ss-BBR dimer
Distance (nm)
1.6
1.2
0.8
0.4
0
10
20
30
40
50
Time (ns)
ICG dimer
Distance (nm)
3.6
2.4
1.2
0.0
0
10
20
30
40
50
Time (ns)

Figure 3

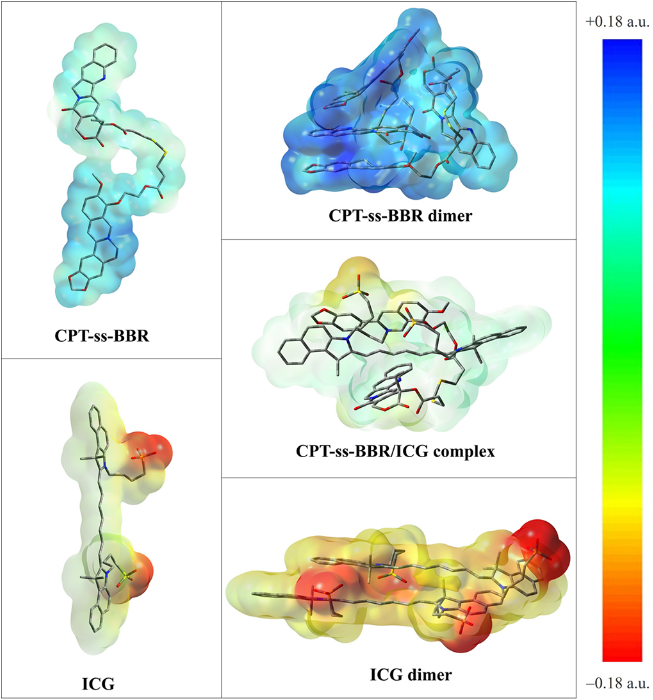

CPT-ss-BBR

CPT-ss-BBR dimer

CPT-ss-BBR/ICG complex

ICG

ICG dimer

Figure 4

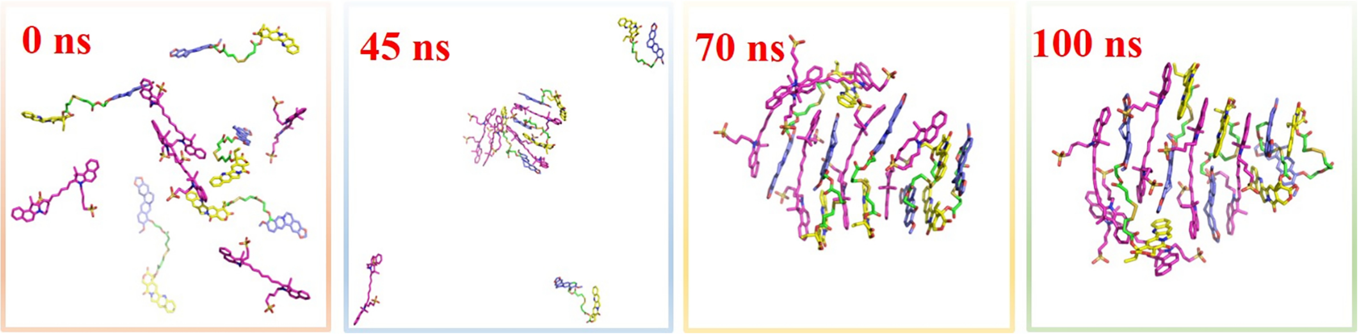

Figure 5

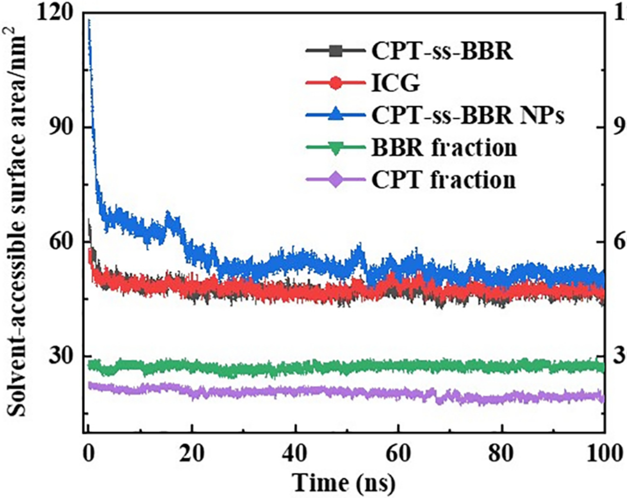

Solvent-accessible surface area/nm$^2$
120
90
60
30
0
20
40
60
80
100
Time (ns)
CPT-ss-BBR
ICG
CPT-ss-BBR NPs
BBR fraction
CPT fraction

Figure 6

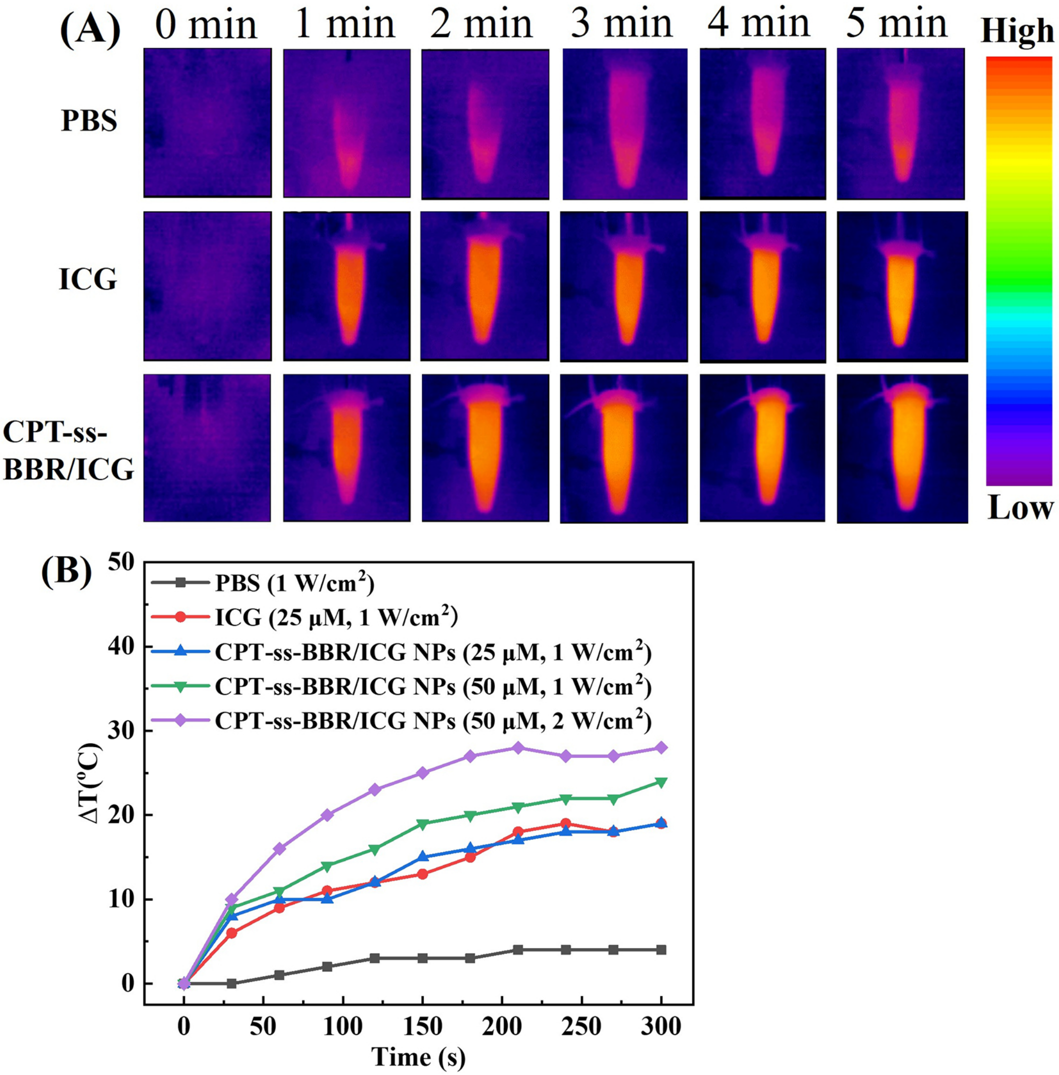
(A)
0 min
1 min
2 min
3 min
4 min
5 min
High
Low
PBS
ICG
CPT-ss-BBR/ICG
(B)
PBS (1 W/cm$^2$)
ICG (25 μM, 1 W/cm$^2$)
CPT-ss-BBR/ICG NPs (25 μM, 1 W/cm$^2$)
CPT-ss-BBR/ICG NPs (50 μM, 1 W/cm$^2$)
CPT-ss-BBR/ICG NPs (50 μM, 2 W/cm$^2$)
ΔT(°C)
0
10
20
30
40
50
Time (s)
0
50
100
150
200
250
300

Figure 7

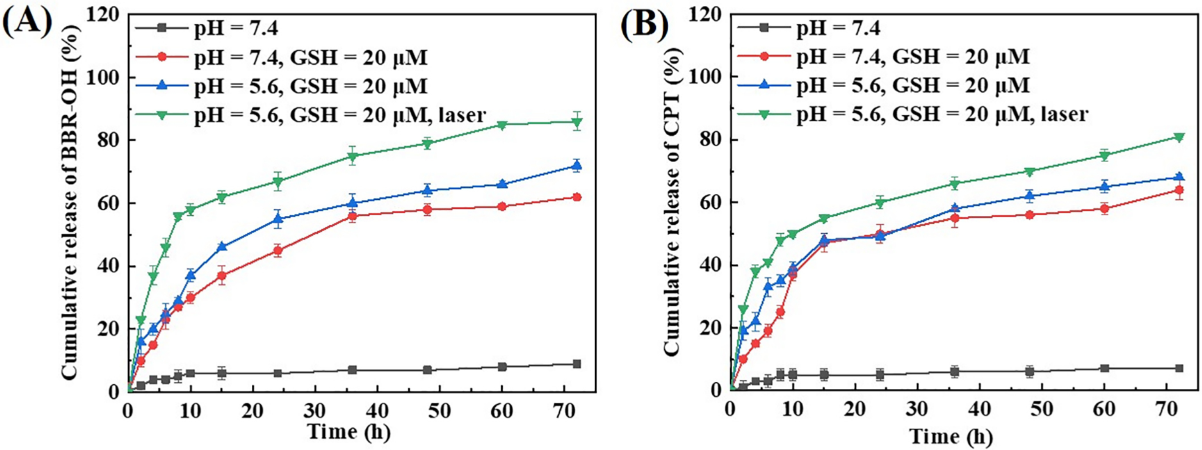
(A)
Cumulative release of BBR-OH (%)
0
20
40
60
80
100
120
Time (h)
0
10
20
30
40
50
60
70
pH = 7.4
pH = 7.4, GSH = 20 μM
pH = 5.6, GSH = 20 μM
pH = 5.6, GSH = 20 μM, laser
(B)
Cumulative release of CPT (%)
0
20
40
60
80
100
120
Time (h)
0
10
20
30
40
50
60
70
pH = 7.4
pH = 7.4, GSH = 20 μM
pH = 5.6, GSH = 20 μM
pH = 5.6, GSH = 20 μM, laser

Figure 8

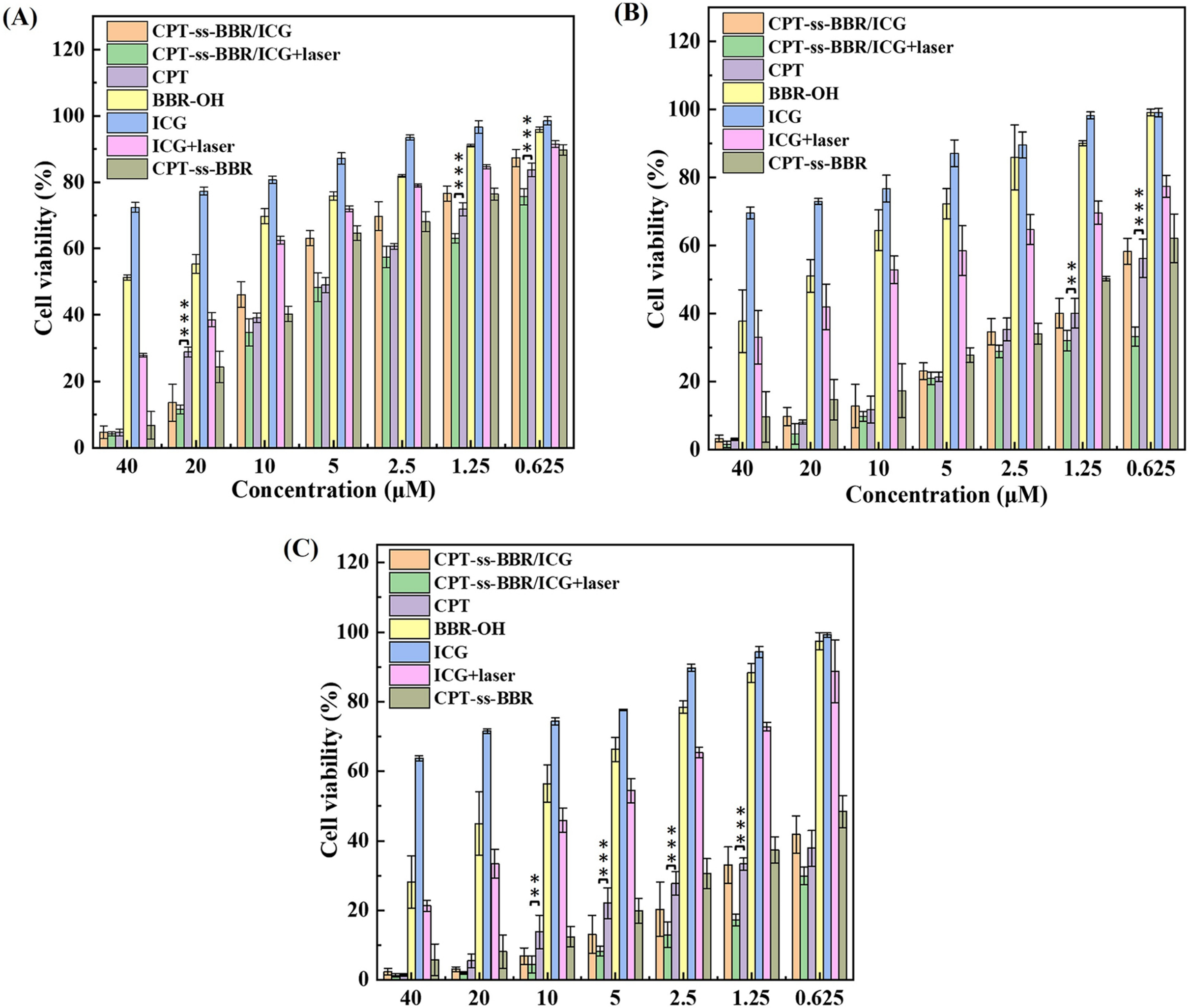
(A)
(B)
(C)
CPT-ss-BBR/ICG
CPT-ss-BBR/ICG+laser
CPT
BBR-OH
ICG
ICG+laser
CPT-ss-BBR
Cell viability (%)
0
20
40
60
80
100
120
40
20
10
5
2.5
1.25
0.625
Concentration (μM)
***
**

Figure 9

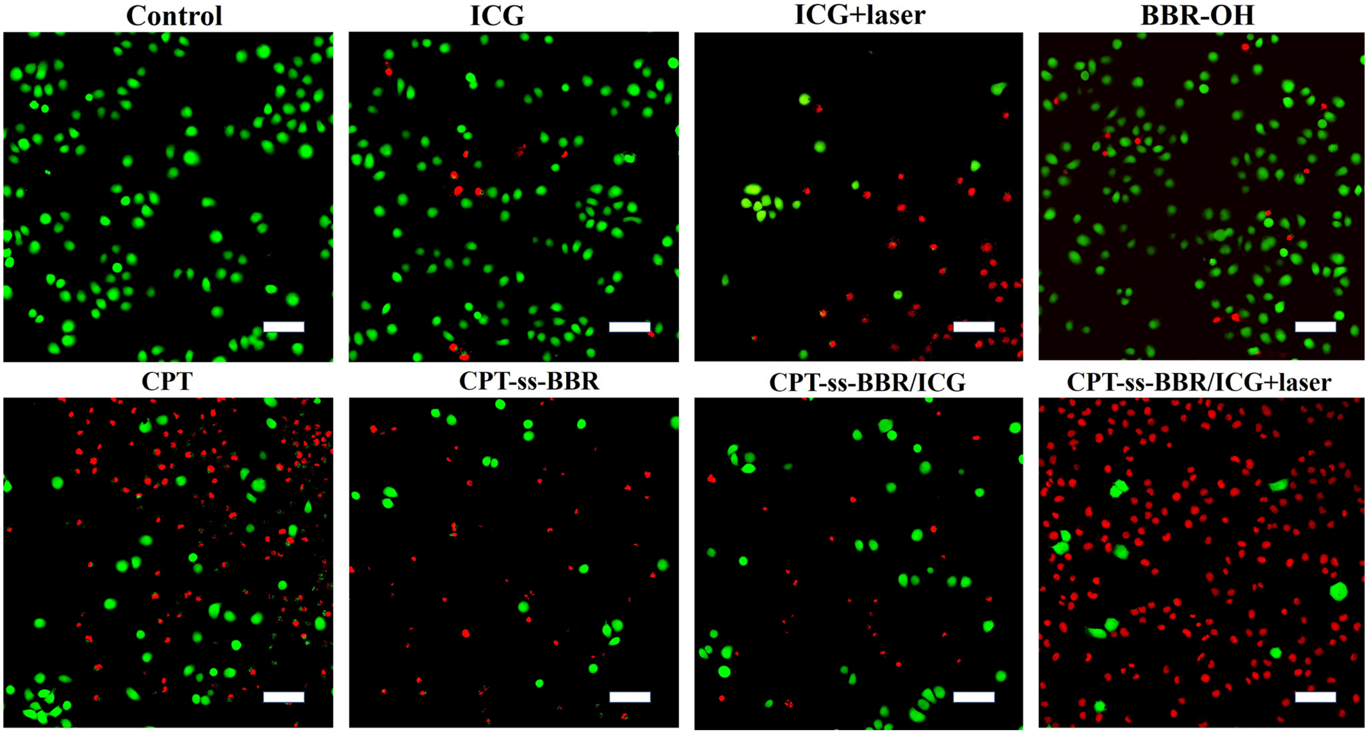
Control
ICG
ICG+laser
BBR-OH
CPT
CPT-ss-BBR
CPT-ss-BBR/ICG
CPT-ss-BBR/ICG+laser

Figure 10

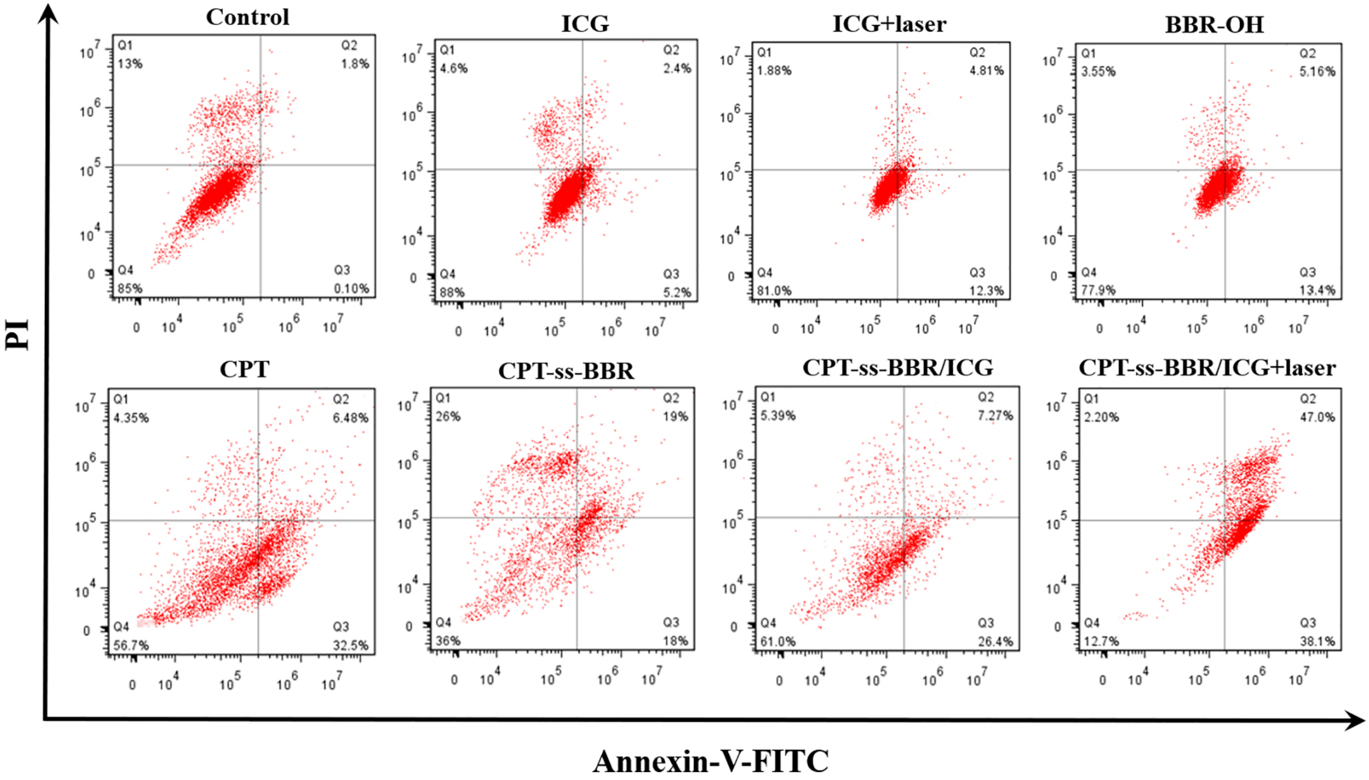
PI
Annexin-V-FITC
Control
Q1 13%
Q2 1.8%
Q4 85%
Q3 0.10%
ICG
Q1 4.6%
Q2 2.4%
Q4 88%
Q3 5.2%
ICG+laser
Q1 1.88%
Q2 4.81%
Q4 81.0%
Q3 12.3%
BBR-OH
Q1 3.55%
Q2 5.16%
Q4 77.9%
Q3 13.4%
CPT
Q1 4.35%
Q2 6.48%
Q4 56.7%
Q3 32.5%
CPT-ss-BBR
Q1 26%
Q2 19%
Q4 36%
Q3 18%
CPT-ss-BBR/ICG
Q1 5.39%
Q2 7.27%
Q4 61.0%
Q3 26.4%
CPT-ss-BBR/ICG+laser
Q1 2.20%
Q2 47.0%
Q4 12.7%
Q3 38.1%
0
$10^4$
$10^5$
$10^6$
$10^7$

Figure 11

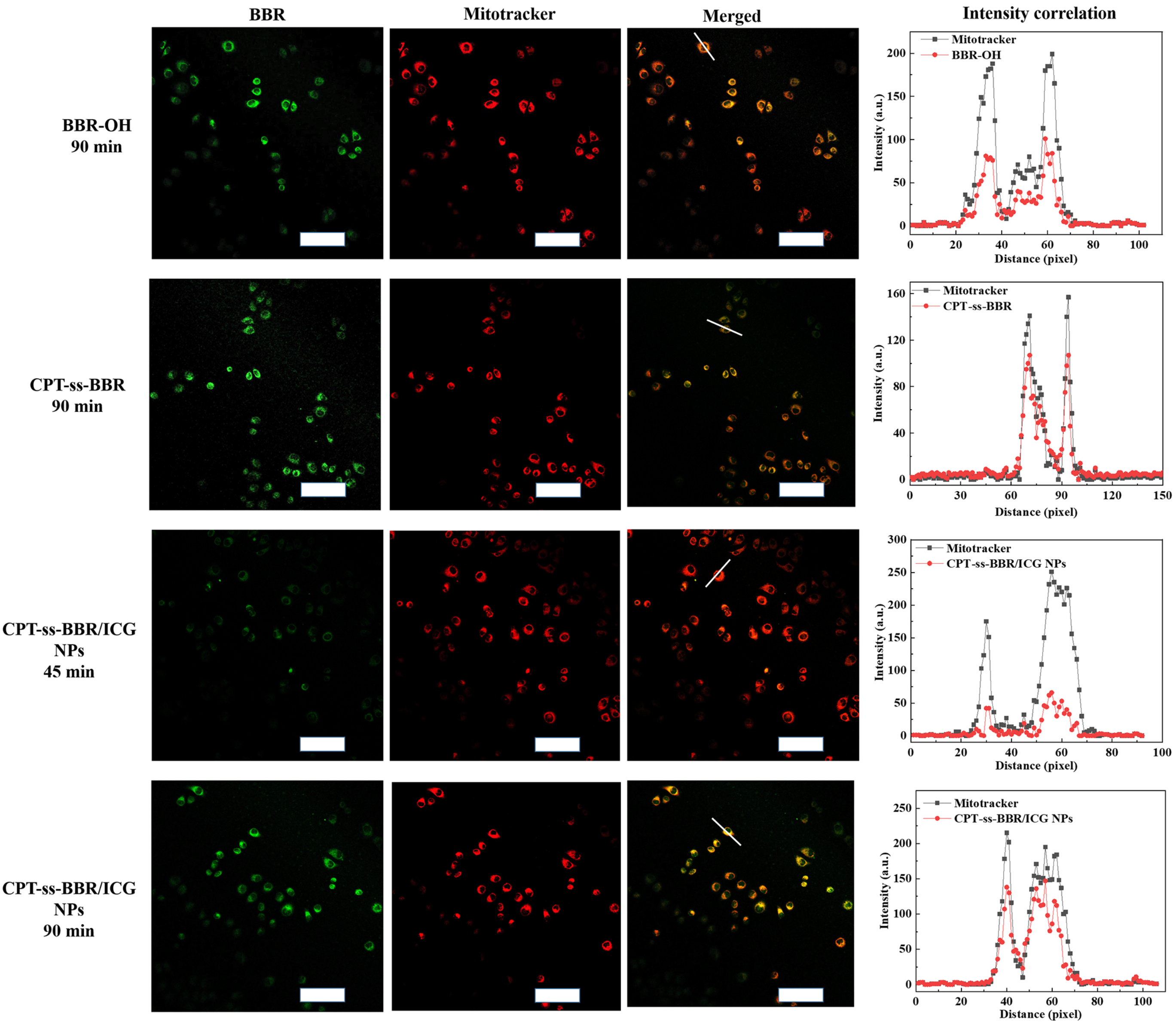
BBR
Mitotracker
Merged
Intensity correlation
BBR-OH
90 min
CPT-ss-BBR
90 min
CPT-ss-BBR/ICG
NPs
45 min
CPT-ss-BBR/ICG
NPs
90 min
Mitotracker
BBR-OH
Mitotracker
CPT-ss-BBR
Mitotracker
CPT-ss-BBR/ICG NPs
Mitotracker
CPT-ss-BBR/ICG NPs
Intensity (a.u.)
Distance (pixel)
0
20
40
60
80
100
30
90
120
150
50
150
200
250
300
160

Figure 12

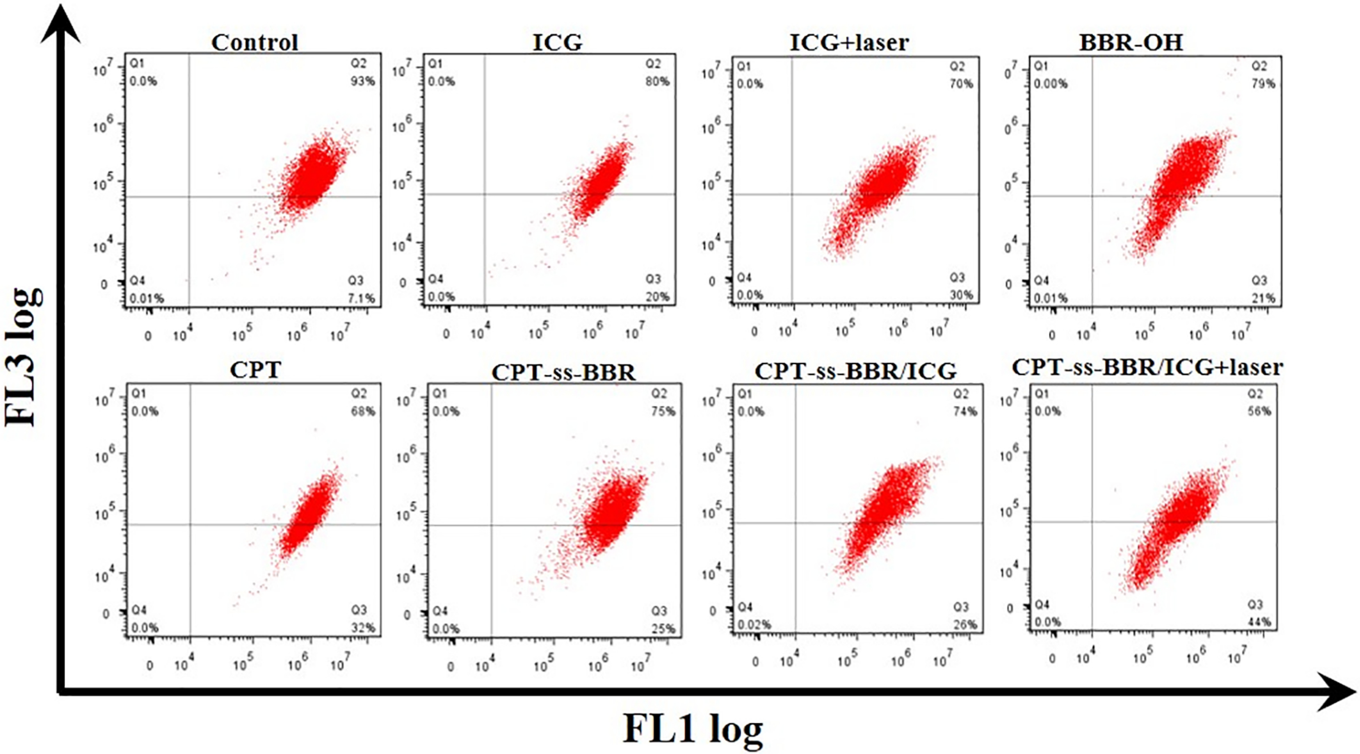
FL3 log
FL1 log
Control
Q1 0.0%
Q2 93%
Q4 0.01%
Q3 7.1%
ICG
Q1 0.0%
Q2 80%
Q4 0.0%
Q3 20%
ICG+laser
Q1 0.0%
Q2 70%
Q4 0.0%
Q3 30%
BBR-OH
Q1 0.00%
Q2 79%
Q4 0.01%
Q3 21%
CPT
Q1 0.0%
Q2 68%
Q4 0.0%
Q3 32%
CPT-ss-BBR
Q1 0.0%
Q2 75%
Q4 0.0%
Q3 25%
CPT-ss-BBR/ICG
Q1 0.0%
Q2 74%
Q4 0.02%
Q3 26%
CPT-ss-BBR/ICG+laser
Q1 0.0%
Q2 56%
Q4 0.0%
Q3 44%
0
$10^4$
$10^5$
$10^6$
$10^7$

Figure 13

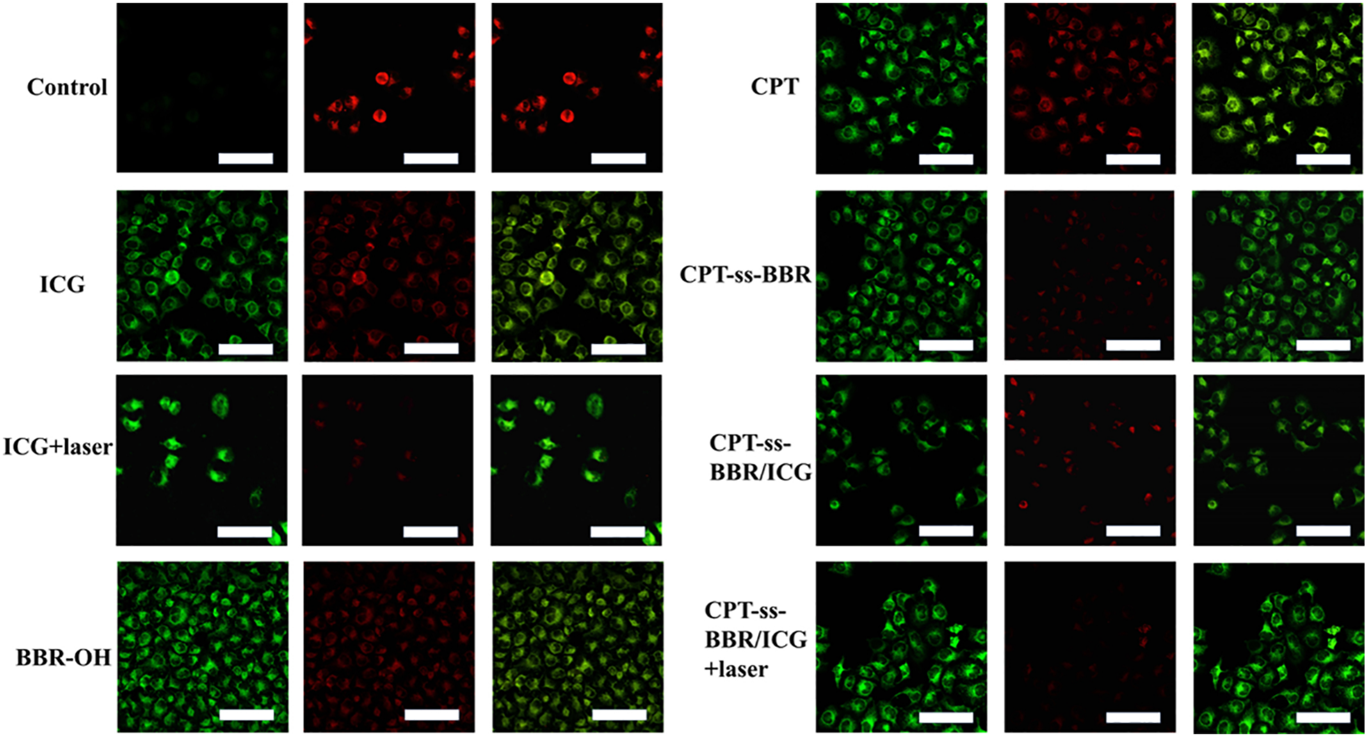
Control
ICG
ICG+laser
BBR-OH
CPT
CPT-ss-BBR
CPT-ss-BBR/ICG
CPT-ss-BBR/ICG +laser

Figure 14

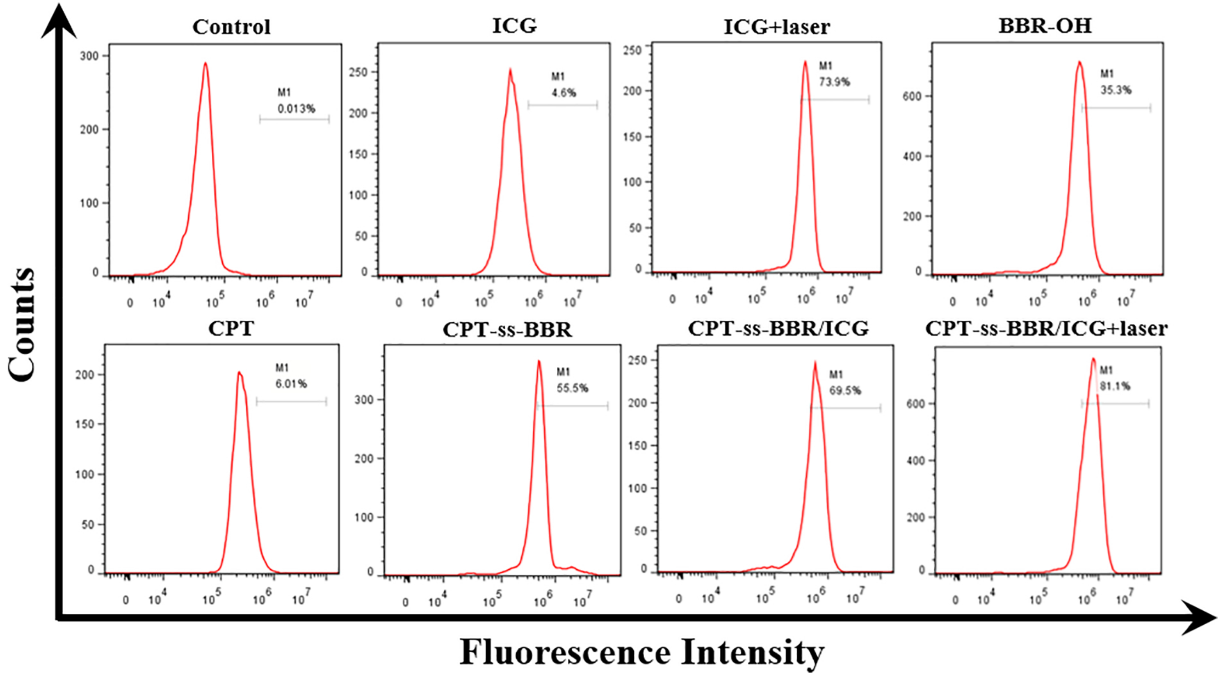
Counts
Fluorescence Intensity
Control
M1
0.013%
ICG
M1
4.6%
ICG+laser
M1
73.9%
BBR-OH
M1
35.3%
CPT
M1
6.01%
CPT-ss-BBR
M1
55.5%
CPT-ss-BBR/ICG
M1
69.5%
CPT-ss-BBR/ICG+laser
M1
81.1%
0
$10^4$
$10^5$
$10^6$
$10^7$

Figure 15

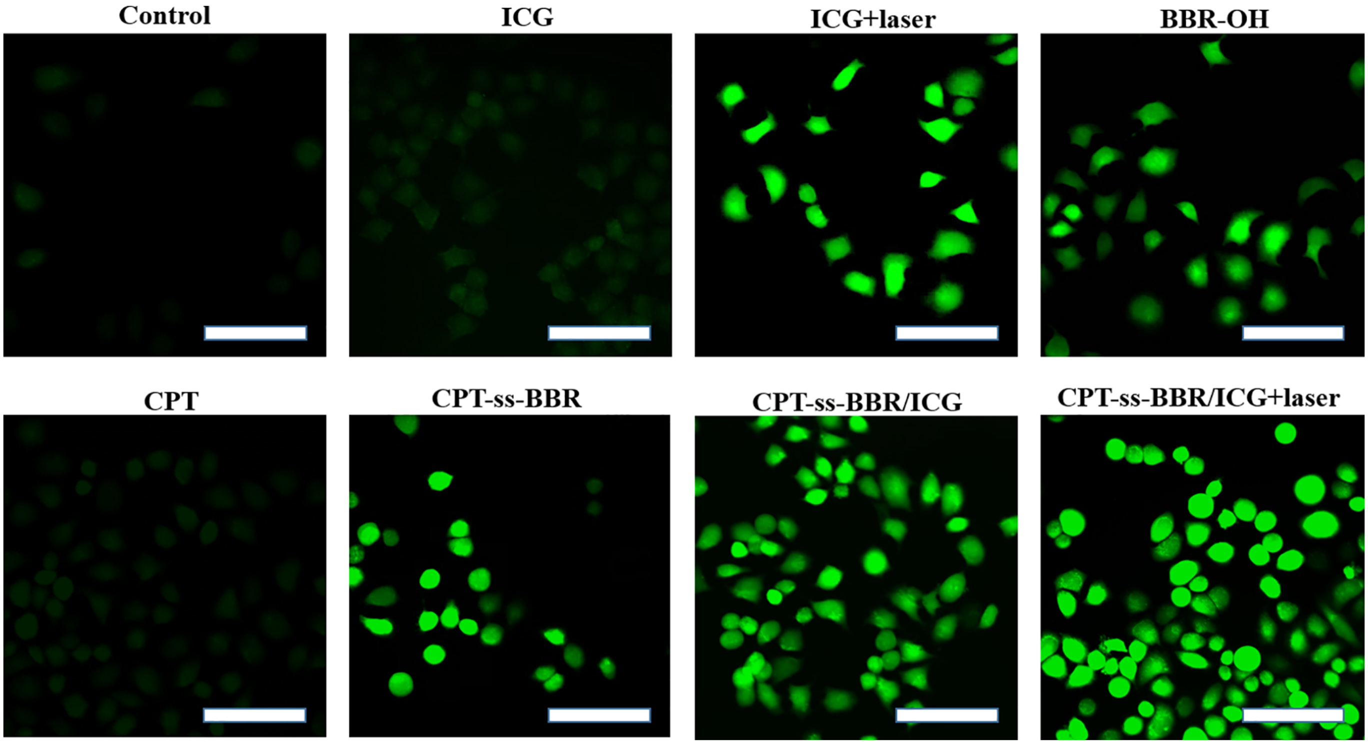
Control
ICG
ICG+laser
BBR-OH
CPT
CPT-ss-BBR
CPT-ss-BBR/ICG
CPT-ss-BBR/ICG+laser

Figure 16